Quaternary Geochronology 83 (2024) 101572

Contents lists available at ScienceDirect

Quaternary Geochronology

journal homepage: www.elsevier.com/locate/quageo

Research paper

Single-grain luminescence and combined U-series/ESR dating of the early Upper Palaeolithic Lagar Velho Rock Shelter, Leiria, Portugal

L.J. Arnold [a,*], M. Demuro [a], M. Duval [b,c,d], R. Grün [b,e], M. Sanz [f,g], A.M. Costa [h,i,j,k], A. C. Araújo [g,h,i], J. Daura [f,g]

[a] School of Physics, Chemistry and Earth Sciences, University of Adelaide, Adelaide, 5005, South Australia, Australia
[b] Centro Nacional de Investigación sobre la Evolución Humana (CENIEH), 09002, Burgos, Spain
[c] Australian Research Centre for Human Evolution (ARCHE), Griffith University, Nathan, 4111, Queensland, Australia
[d] Department of Archaeology and History, La Trobe University, Melbourne Campus, Bundoora, 3086, Victoria, Australia
[e] Research School of Earth Sciences, Australian National University, Acton, 0200, Australian Capital Territory, Australia
[f] Grup de Recerca del Quaternari (GRQ-SERP), Departament d'Història i Arqueologia, Universitat de Barcelona, 08001, Barcelona, Spain
[g] UNIARQ-Centro de Arqueologia da Universidade de Lisboa, Universidade de Lisboa, 1600-214, Lisbon, Portugal
[h] Laboratório de Arqueociências (LARC)-DGPC, 1300-418, Lisbon, Portugal
[i] InBIO Laboratório Associado, BIOPOLIS - Programme in Genomics, Biodiversity and Land Planning, CIBIO - Centro de Investigação em Biodiversidade e Recursos Genéticos, Universidade do Porto, Vairão, Portugal
[j] IDL - Instituto Dom Luiz, Universidade de Lisboa, 1749-016, Lisbon, Portugal
[k] IIIPC - Instituto Internacional de Investigaciones Prehistóricas de Cantabria, Universidad de Cantabria - Gobierno de Cantabria-Santander, 39005, Santander, Spain

ARTICLE INFO

Keywords:
Single-grain OSL
Single-grain TT-OSL
Combined U-Series/ESR
Gravettian
Solutrean
Iberian Peninsula
Upper palaeolithic

ABSTRACT

The existing radiocarbon (^{14}C) dating framework for Lagar Velho is broadly consistent but provides limited constraint on several geoarchaeological complexes (GCs) and does not favour detailed chronological comparisons across all sectors of the site; including the stratigraphically disconnected child burial complex in the east area and the broader archaeological sequence in the central-west area. In this study, we undertake a complementary chronological assessment of Lagar Velho Rock Shelter using single-grain quartz OSL, single-grain quartz TT-OSL and combined U-series/ESR dating of fossil teeth, with the aim of establishing more comprehensive reconstructions of archaeological events and placing the human occupation sequence in a firmer regional climatic context. Expanding on the original chronological study, we also compare the published ^{14}C datasets against widely used sample quality indicators (i.e., organic preservation and contamination proxies) to ensure reliable comparisons with our new luminescence and combined U-series/ESR ages. Eight ^{14}C samples pass our combined chronological and stratigraphic hygiene criteria and are included in the final dating evaluations. Ten of the twelve optical dating samples produce homogeneous equivalent dose (D_e) datasets indicative of suitable daylight exposure. The replicate single-grain TT-OSL D_e datasets exhibit more pronounced scatter, consistent with enhanced potential for insufficient bleaching of TT-OSL residual doses in some karst settings. The fossil enamel samples dated using U-series/ESR span relatively low natural dose ranges, necessitating the inclusion of maximum dose (D_{max})-adjusted dose response curve fitting and additional background noise subtraction to avoid D_e biases of up to 13%. Stratigraphically consistent ages ($n = 26$) spanning the full archaeological infill sequence are obtained using the four different dating methods, providing a robust interpretive framework and underscoring the significant role of single-grain OSL and combined U-series/ESR dating for refining early Upper Palaeolithic histories of Iberia. Bayesian modelling of the combined chronological dataset reveals a site accumulation history spanning 35,750–23,440 cal. BP and provides improved age constraints on all GCs; particularly the *al*, *bs*, *tc*, *gs* and *ls* deposits that were previously undated or imprecisely constrained. The age of the child burial complex is refined to 29,410–28,280 cal. BP, potentially occurring within Greenland Interstadial 4. Comparison of the modelled GC ages from the east and west-central areas enables improved temporal correlations of depositional events across stratigraphically disconnected sectors of the site. This analysis suggests that the child burial complex and the Late Gravettian occupation are statistically indistinguishable based on current dating evidence. The new dating assessments reveal three periods of human occupation at Lagar Velho: the Late

* Corresponding author.
E-mail address: lee.arnold@adelaide.edu.au (L.J. Arnold).

https://doi.org/10.1016/j.quageo.2024.101572
Received 13 November 2023; Received in revised form 19 April 2024; Accepted 10 June 2024
Available online 23 June 2024

Gravettian (including the shorter duration child burial event) 31.6–26.0 ka from the end of Heinrich Stadial (HS) 3 until the emergence of HS2; the Terminal Gravettian 26.5–24.5 ka coinciding with HS2; and the Middle Solutrean 25.2–23.4 ka extending from HS2 to the end of Greenland Stadial 3. The timing of these occupations during late Marine Isotope Stage (MIS) 3 and early MIS 2 highlights the significance of central western Portugal for supporting regional human populations during periods when much of Europe was experiencing extreme cold, aridity and expanded glacial coverage.

1. Introduction

Lagar Velho Rock Shelter, Leiria, central-western Portugal (Fig. 1), is a key locality for understanding the early Upper Palaeolithic history of Southwest Europe from both an anthropological and cultural perspective (Zilhão and Trinkaus, 2002). The site preserves the near-complete skeleton of a 4-year-old buried child (Duarte et al., 1999; cf. Tattersall and Schwartz, 1999), which was ritually interred in a recess of the rock shelter with pierced shell ornamentation, red deer teeth and red ochre. The child burial complex is part of a ~5m infill sequence containing successive Late Gravettian, Terminal Gravettian (Proto-Solutrean) and Middle Solutrean occupation layers (Zilhão and Trinkaus, 2002; Almeida et al., 2009). In addition to capturing the Gravettian–Solutrean transition, Lagar Velho preserves an extensive Late Gravettian living floor with separate hearth features, faunal processing areas and concentrations of refitting lithic artefacts (Zilhão and Trinkaus, 2002; Almeida et al., 2009). This structured occupation surface provides unique insights into recurrent site use, planning and organisation strategies, and division of functional activities by the early Upper Palaeolithic inhabitants (Almeida et al., 2009).

The existing site chronology is based on ^{14}C dating of charcoal and bone from different sectors of the rock shelter (Zilhão and Trinkaus, 2002), which constrains the Late Gravettian to Middle Solutrean archaeological layers to between 23,170 ± 140 and 20,220 ± 180 ^{14}C yr BP (27.7–27.2 to 24.8–23.8 ka cal. BP; 95.4% C.I. calibrated ranges; Reimer et al., 2020) and reveals the broader infill sequence extends back at least 29,800 ± 2500 ^{14}C yr BP (43.1–29.9 ka cal. BP). The ^{14}C ages for the child burial complex span 24,860 ± 200 to 23,920 ± 220 ^{14}C yr BP (29.7–28.7 to 28.6–27.7 ka cal. BP), consistent with the Gravettian traits of the associated burial ornamentation (e.g., d'Errico and Vanhaeren, 2015). While the combined ^{14}C dataset is stratigraphically consistent, several of the main depositional units remain undated or imprecisely constrained, and the ^{14}C ages are primarily based on standard (acid--base-acid; ABA) pre-treatment procedures, which may not be ideally suited for complete removal of organic contaminants in some Late Pleistocene settings (e.g., Demuro et al., 2019a, 2023; Zilhão et al., 2020, 2021a) compared to more rigorous ^{14}C extraction procedures (i.e., ultrafiltration and ABOx-SC; Bird et al., 1999; Brock et al., 2007). Careful examination of the originally reported ^{14}C data against widely used sample quality indicators (i.e., organic preservation and contamination proxies) may therefore be required to ensure reliable interpretations of the existing ^{14}C dataset.

A key focus of ongoing research at Lagar Velho is establishing firmer chronostratigraphic correlations between different sectors of the site, which remain tentative owing to lateral variations and anthropic truncation of the longitudinal profile. In particular, the relationship between the child burial complex in the east area and the broader archaeological and sedimentary sequence in the central-west area (Fig. 1) is uncertain as 2–3 m of original infill was largely removed during pre-discovery terracing activities and initial salvage excavations (Zilhão and Trinkaus, 2002). Consequently, there is no continuous longitudinal record of the entire succession preserved across all sectors. Clarification is also needed regarding the chronostratigraphic relations of the basal deposits preserved in the east and central-west areas, which exhibit different sedimentological characteristics and lack direct stratigraphic connections but potentially represent pene-contemporaneous facies (Zilhão and Trinkaus, 2002).

These correlative uncertainties and the current reliance on a single dating technique mean there is a need to expand and complement the Lagar Velho chronological framework using a broader suite of methods. In this paper, we present results of a systematic optical dating study and an initial combined uranium series and electron spin resonance (ESR) dating examination of the site, which aims to establish more comprehensive reconstructions of archaeological events and their relations with Late Pleistocene climate change. To achieve the main study aim of improved chronostratigraphic evaluations of the anthropological remains, broader archaeological succession and combined infill sequence, we focus on the following specific objectives: (i) Establish depositional ages for all excavated units using single-grain OSL and combined U-series/ESR dating; (ii) assess the suitability of single-grain TT-OSL for dating Late Pleistocene deposits at the site; (iii) evaluate the quality of existing ^{14}C results, and examine the consistency of ages obtained using different dating techniques; (iv) examine chronostratigraphic correlations across different sectors by combining all reliable dating evidence in Bayesian models.

2. Site overview, sample details and experimental procedures

Lagar Velho Rock Shelter, located near the mouth of the Lapedo Valley gorge (39°45′25″N; 8°43′58″W; 83m a.s.l.) on the southern banks of the Caranguejeira stream, contains an elongated north-facing platform spanning ~125 m^2. Fig. 1 shows a schematic plan view of the rock shelter, highlighting the gridded reference scheme, excavation areas and locations of the different sectors examined in this dating study. The excavated stratigraphic succession has been sub-divided into a series of geoarchaeological complexes (GCs) based on relative positioning, pedosedimentary characteristics and anthropic features (Zilhão and Trinkaus, 2002). In the central-west area, the lower GCs are alluvial accumulations (*al*) and "transitional" deposits (*tc*) comprising gravity-derived sediments and alternating alluvial input, while the upper GCs (*us*, *ms*, *ls*) represent slopewash deposits and gravity-driven sediments. Much of the *us* and *ms* deposits in the central-west area have been removed by terracing activities, though a hanging remnant of the uppermost original profile is preserved along a recess of the shelter back wall (Testemunho Pendurado; TP sector) (Fig. 1). The east area succession is dominated by slopewash and gravity-driven accumulations (*bs*, *gs*), as well as transitional slopewash–fluviatile *tc* deposits (Table S1), but the original upper profile has been truncated by terracing activities.

In terms of cultural association, the *us* deposits contain successive Terminal Gravettian and Middle Solutrean occupations, while the *ms* and upper *ls* deposits preserve the main phase of repeated Late Gravettian occupation (Table S1). The child burial complex is inset into the upper part of the *gs* deposit in the east area. However, lack of direct lateral continuity means the exact relationships between the child burial in the east and the *us–ms–ls* archaeological occupations in the central-west are yet to be defined (Zilhão and Trinkaus, 2002; Almeida et al., 2009). The overall stratigraphic integrity of the sequence is supported by exceptionally high artefact refitting percentages from the Late Gravettian occupation floor (Almeida et al., 2009), as well as the presence of well-preserved boundaries between many of the GCs. Owing to the absence of a continuous longitudinal record of the succession across all sectors, we have not assumed any prior correlative relationships of GCs between the east and central-west areas in the present dating study.

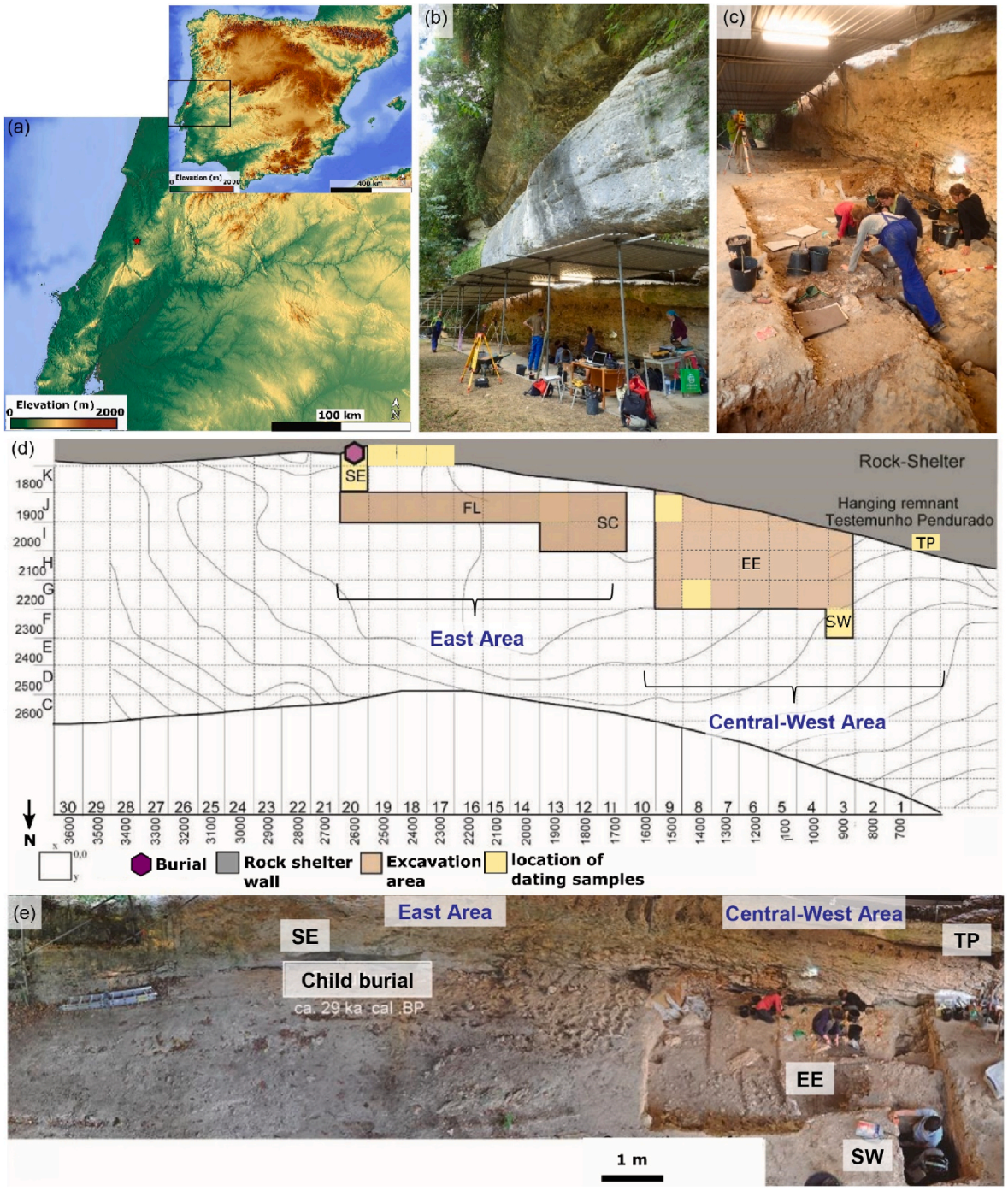

Fig. 1. Overview and location of the Lagar Velho Rock Shelter. (a) Main plot and inset map: Location of Lagar Velho Rock Shelter in the Estremadura region of central-western Portugal (source: Google Earth image with Maps-For-Free relief Overlay: http://ge-map-overlays.appspot.com/world-maps/maps-for-free-relief). (b) photograph of the rock shelter looking towards the east (photo credit: Lee Arnold). (c) photograph of the ongoing excavations in the EE sector (photo credit: Lee Arnold). (d) schematic plan view of the rock shelter, highlighting the gridded reference scheme, excavation areas and locations of the different sectors examined in this dating study. (e) aerial photograph of the exposed sedimentary profiles, showing the locations of the different areas and sectors examined in this dating study (modified from Sanz et al., 2023).

Consequently, these two areas of the site are considered separately for Bayesian chronostratigraphic modelling purposes.

Single-grain optically stimulated luminescence (OSL) dating of quartz (e.g. Murray et al., 2021) offers the advantage of establishing direct depositional ages on the fossil- and archaeology-bearing sediment layers, and is therefore well-suited for refining the chronological relationships of deposits preserved across different sectors of Lagar Velho. Single-grain thermally transferred OSL (TT-OSL) provides a means of establishing complementary quartz depositional ages at the site using a semi-independent luminescence signal, and this technique has recently been used to establish reliable chronologies at a range of Iberian Lower and Middle Palaeolithic sites (e.g. Arnold et al., 2013, 2014, 2015; Demuro et al., 2014, 2019b, 2020a, 2020b, 2022; Zilhão et al., 2021a; Duval et al., 2022). However, the relatively slow bleaching characteristics of TT-OSL signals (on the order of days compared to seconds for the fast component OSL signal; Demuro et al., 2015; Duval et al., 2017;

Arnold et al., 2019) may mean that higher residual doses and age overestimation are potential problems in Upper Palaeolithic settings (Demuro et al., 2019a; Arnold et al., 2022). An additional objective of this study is therefore to examine single-grain TT-OSL signal resetting characteristics in a Late Pleistocene karstic setting using assessments of comparative quartz luminescence signals that bleach at different rates. Finally, the presence of well-preserved faunal remains throughout much of the Lagar Velho sequence opens up the possibility of using combined U-series/ESR analysis to directly date herbivore teeth and independently evaluate the consistency of existing ^{14}C bone ages.

Twelve luminescence dating samples were collected from four sectors (TP, EE, SW, SE) spanning the east and central-west areas of the rock shelter, as shown in Fig. 1 and Fig. S1. At least one sample was collected from each excavated GC inside the rock shelter (Table S1) to help constrain the chronological relationships of the full range of deposits preserved across different sectors. Single-grain OSL dating was applied to all twelve samples, with comparative single-grain TT-OSL measurements performed on a representative subset of four samples from the east area (Table S1) owing to the significantly longer machine time requirements of TT-OSL dating. The OSL and TT-OSL dating procedures employed in this study are based on Arnold et al. (2019, 2022) and Demuro et al. (2015, 2023), with additional details provided in the Supplementary Information (Figs. S2–5; Tables S2–S4). Equivalent dose (D_e) values have been determined for individual quartz grains using the single-aliquot regenerative-dose (SAR) procedures shown in Table S2, which yielded suitable dose-recovery test results for sample ALV18-3 (Fig. S3). The environmental dose rates for the luminescence dating samples have been calculated using a combination of *in situ* field gamma-ray spectrometry (Arnold et al., 2012b; Duval and Arnold, 2013) and low-level beta counting.

Combined U-series/ESR dating was performed on the M3 molar of a deer mandible fragment found immediately behind luminescence sample ALV18-7 in the SW sector *al* deposits (Table S1; Fig. S6). Two replicate samples (POR1801A and POR1801B) were dated from different parts of the deer molar (Fig. S6) using standard enamel powder U-series/ESR dating procedures (e.g., Duval et al., 2019), which are further detailed in the Supplementary Information (Figs. S6–8; Tables S5–S8). D_e values were determined using the multiple aliquot additive dose (MAAD) method applied to natural and gamma dosed aliquots. Laser ablation (LA) U-series analyses were carried out using the equipment, principles and procedures outlined in Eggins et al. (2003, 2005) and Grün et al. (2014). Environmental gamma and beta dose rates were derived from the *in situ* field gamma spectrometry measurements of paired luminescence sample ALV18-7 and laboratory-based high-resolution gamma spectrometry, respectively. The U concentrations of dental tissues, enamel internal dose rates and dentine beta dose rates were determined using LA U-series and solution ICP-MS data, as detailed in the Supplementary Information. Combined U-series/ESR age calculations were performed using either the DATA (Grün, 2009) or USESR (Shao et al., 2014) programs.

Bayesian age modelling has been used to derive combined chronologies for individual GCs and to integrate the single-grain OSL, single-grain TT-OSL, U-series/ESR and ^{14}C ages within a unified chronostratigraphic framework. Separate Bayesian models were constructed for the GC successions preserved in the central-west and east areas, incorporating all radiometric dating results (likelihoods) considered reliable in this study, together with all known stratigraphic information (priors) for the site. Bayesian modelling was undertaken using OxCal v4.4 (Bronk Ramsey, 2009) and is based on the approach outlined in Demuro et al. (2019b, 2020a), Zilhão et al. (2021b), and Fusco et al. (2023) (see Supplementary Information and Tables S9–S10 for further details).

3. ^{14}C dating evaluations

An important aspect of our comparative chronology study at Lagar Velho is re-evaluating the reliability of existing ^{14}C results using widely employed sample purity and quality assurance criteria (e.g., Pettitt et al., 2003; Wood et al., 2013; Talamo et al., 2021). For this purpose, we have compared the originally published ^{14}C datasets from Zilhão and Trinkaus (2002) with the well-established ^{14}C analytical indicator thresholds detailed in van Klinken (1999) and Rebollo et al. (2011). Unfortunately, the limited information published with the original ^{14}C datasets precludes consideration of a broader suite of chemical indicators such as % collagen, δ^{13}C and δ^{15}N. Bone collagen samples with C:N ratios falling outside the range of 2.9–3.6 are considered unsuitable for dating as they are potentially indicative of diagenetic alteration or the presence of exogenous contaminants (Ambrose, 1990; van Klinken, 1999). Genuine wood charcoal samples are expected to yield C combustion yields of 50–70% (Braadbaart and Poole, 2008; Braadbaart et al., 2009); samples with C combustion yields <50% are therefore considered unreliable owing to the presence of extraneous (non-charcoal) material that may promote introduction of contaminants (Rebollo et al., 2011).

Table 1 summarises the ^{14}C samples considered by Zilhão and Trinkaus (2002) as being stratigraphically and methodological reliable (i.e., sourced from *in situ* deposits and using materials that were not treated with organic consolidants prior to field extraction). The originally reported 95.4% calibrated age ranges have also been recalculated using IntCal20 (Reimer et al., 2020) to enable more appropriate chronological comparisons with our new luminescence and combined U-series/ESR datasets. Sixteen ^{14}C ages satisfy the original authors' pre-selection criteria, collectively constraining the Lagar Velho sedimentary sequence to between 43.1–29.9 and 24.8–23.8 ka cal. BP. Examination of the available quality assurance data reveals that two of these charcoal samples (OxA-8420, GrA-13310) and two burnt bone samples (OxA-9571, OxA-9572) lie outside of the standard C:N and %C acceptance ranges, while a third burnt bone sample (Beta-139361) was flagged as suffering exogenous carbon contamination in the original laboratory report and consequently yields a non-finite (minimum) age. Two additional ^{14}C samples analysed via commercial analyses (Wk-9256, Wk-9571) are lacking methodological details and chemical indicators, and were not included in the main ^{14}C evaluation study for the site (Pettitt et al., 2002). These two samples therefore fail the minimum reporting requirements for our quality assurance assessments. In total, our ^{14}C chronological hygiene assessments reveal that 50% of the charcoal samples, 40% of the bone samples, and 100% of the burnt bone samples shown in Table 1 suffer potential contamination or preservation issues, or lack sufficient analytical indicators to ensure meaningful evaluations of sample purity and methodological suitability.

Of the nine ^{14}C samples that satisfy the collagen and C yield quality assurance criteria, one sample (OxA-10674) is taken from a sector not examined in the present dating study (SC sector) (Table 1; Fig. 1) and therefore its stratigraphic relationship with our luminescence and combined U-series/ESR dating samples has not been directly evaluated. Moreover, all other ^{14}C samples collected from the SC sector yield problematic results (Beta-139361) or fail the standard analytical quality assurance criteria (OxA-9571, OxA-9572), suggesting that this profile may have experienced a potentially complex diagenetic history. To avoid introducing uncertainties in assigned stratigraphic relationships or possible inconsistencies with ordering of Bayesian modelled events, we have restricted consideration of dating results to the four main sectors (TP, EE, SW and SE sectors) that were sampled in the current study. Eight ^{14}C samples therefore pass our combined chronological and stratigraphic hygiene criteria and are included in the final comparative dating evaluations (Table 1).

4. Optical dating results

Table 2 summarises the environmental dose rates, single-grain OSL and TT-OSL D_e values and final ages for the twelve luminescence dating samples. Between 6 and 16% of OSL D_e measurements per sample and

Table 1
Sample quality evaluations of the accelerator mass spectrometry (AMS) and liquid scintillation counting (LSC)^{14}C results from the central-west and east areas of Lagar Velho Rock Shelter. Percentage carbon combustion yields have been calculated from the burnt weight (mg) and carbon yield (mg) data provided in Table A7.4 of Zilhão and Trinkaus (2002). The samples included in this summary are limited to those collected from stratigraphically reliable (i.e., *in situ*, non-reworked) deposits and those that were not subjected to organic consolidant treatment prior to selection for dating analysis. These pre-screening criteria have resulted in the elimination of four charcoal samples (OxA-8418, OxA-8424, OxA-8425, OxA-8426) that were originally flagged by Zilhão and Trinkaus (2002) as being derived from redeposited fill material in erosion channels of the TP sector. Similarly, three bone collagen samples GrA-10972, GrA-12194, GrA-13360 have not been included because they were originally treated in the field with an organic consolidant/glue. The presence of soluble contaminants cannot be excluded with these three samples, especially as a less stringent version of the ABA pre-treatment was needed owing to the poorly preserved nature of the fossil remains.

Area	sector	GC	Sample ID	Material	Pretreat-ment[a]	Method	Age (^{14}C yr BP)[b]	Age (cal. BP 95% CI)[c]	C:N ratio	C yield (%)	Sample purity/analytical quality rating
central-west	TP	us	OxA-8419	Charcoal, unidentified single piece	ABA	AMS	20220 ± 180	24823–23841		61.9	pass
			Sac-1561	Charcoal, unidentified multiple fragments	ABA	LCS	21380 ± 810	27341–23876		54.6	pass
			OxA-8420	charcoal, unidentified single piece	ABA	AMS	21180 ± 240	25936–25008		2.1	fail: C yield <50%
central-west	TP	ms	OxA-10303	Charcoal, *Pinus sylvestris* single piece	ABA	AMS	22390 ± 280	27229–26049		53.3	pass
central-west	SW		Wk-9256	Charcoal, *Pinus sylvestris*	ABA	AMS	22493 ± 107	27121–26436		–	fail: quality indicators not reported. Methodological details not provided.
east	SC		OxA-9571	burnt bone, *Equus* sp. phalanx	ABA	AMS	23130 ± 130	27686–27225	7.2		fail: C:N > 2.9–3.6
east	SC	ls	OxA-9572	burnt bone, unidentified	ABA	AMS	23170 ± 140	27708–27240	7.5		fail: C:N > 2.9–3.6
			Beta-139361	burnt bone, unidentified	ABA	AMS	>22720	>22720	–		fail: possible exogenous C reported. Methodological details not provided.
central-west	SW		Wk-9571	Bone, unidentified	ABA	AMS	23042 ± 142	27700–27224	–		fail: quality indicators not reported. Methodological details not provided.
east	SC	tc	OxA-10674	Bone, *Equus* sp. metapodial diaphysis	UF	AMS	24950 ± 230	29857–28756	2.9–3.6[d]		pass[e]
central-west	SW	al	OxA-11318	Bone, *Equus* sp. mandible	UF	AMS	29800 ± 2500	43132–29869	2.9–3.6[d]		pass
east	SE	child burial	OxA-8422	Bone, *Oryctolagus* vertebra	ABA	AMS	23920 ± 220	28640–27727	3.3		pass
			OxA-8423	Bone, *Cervus* sp. third phalanx	ABA	AMS	24520 ± 240	29210–28080	3.3		pass
			OxA-8421	Bone, *Cervus* sp. os coxae	ABA	AMS	24660 ± 260	29633–28233	3.2		pass
			GrA-13310	Charcoal, *Pinus sylvestris* single branch	ABA	AMS	24860 ± 200	29699–28694		41.5	fail: C yield <50%
east	SE	tc-bs	OxA-10849	Bone, *Equus* sp. or *Cervus* sp. long bone fragment	UF	AMS	27100 ± 900	33915–29834	3.0		pass

[a] ABA = acid-base-acid pre-treatment with no ultrafiltration; UF = acid-base-acid pre-treatment with ultrafiltration.
[b] Uncalibrated^{14}C age uncertainties presented at 1σ.
[c] Calibrated age presented at 95.4% probability range. Calibration has been undertaken using OxCal 4.4 (Bronk Ramsey, 2009) and IntCal20 (Reimer et al., 2020).
[d] The specific C:N ratios of these two samples were not provided in Zilhão and Trinkaus (2002). However, the C:N ratios were reported as falling within the laboratory threshold range (i.e., 2.9–3.6).
[e] Note - Sector SC was not sampled as part of our comparative dating evaluations. The stratigraphic relationships of OxA-10674 and the luminescence and combined U-series/ESR dating samples collected in this study have therefore not been directly evaluated.

Table 2
Single-grain OSL and single-grain TT-OSL dating results for the Lagar Velho samples.

Sample	Area	Sector	GC	Grain size (μm)	Water content (%) [a]	Environmental dose rate (Gy/ka)				Equivalent dose (D_e) data					Age (ka) [f,l]
						Beta dose rate [b]	Gamma dose rate [c]	Cosmic dose rate [d]	Total dose rate [e,f]	D_e type [g]	No. Of Grains [h]	OD (%) [i]	Age model [j,k]	D_e (Gy) [f]	
ALV18-1	central-west	TP	us	212–250	3.9/14.9	0.65 ± 0.03	0.71 ± 0.03	0.06 ± 0.01	1.46 ± 0.08	SG OSL	366/2400	29 ± 1	MAM-3	36.0 ± 0.9	24.6 ± 1.5
ALV18-2	central-west	TP	ms	212–250	4.5/14.9	0.89 ± 0.05	0.96 ± 0.04	0.06 ± 0.01	1.95 ± 0.10	SG OSL	391/2400	29 ± 2	CAM	49.0 ± 0.9	25.1 ± 1.5
ALV18-3	central-west	EE	ms	212–250	8.4/13.8	1.36 ± 0.07	0.93 ± 0.03	0.07 ± 0.01	2.40 ± 0.12	SG OSL	180/1300	28 ± 2	CAM	67.5 ± 1.8	28.2 ± 1.7
				90–125	8.4/13.8	1.46 ± 0.07	0.93 ± 0.03	0.07 ± 0.01	2.49 ± 0.13	SG TT-OSL	115/3700	49 ± 6	MAM-3	75.9 ± 6.1	30.5 ± 3.0
ALV22-5	central-west	EE	ms	212–250	15.8/15.8	0.74 ± 0.04	0.59 ± 0.02	0.06 ± 0.01	1.43 ± 0.08	SG OSL	322/2000	26 ± 2	CAM	41.6 ± 0.8	29.0 ± 1.7
ALV18-4	central-west	SW	ms	212–250	14.7/14.7	1.33 ± 0.07	0.82 ± 0.03	0.06 ± 0.01	2.25 ± 0.12	SG OSL	379/2400	27 ± 2	CAM	69.9 ± 1.3	31.1 ± 1.8
				90–125	14.7/14.7	1.43 ± 0.07	0.82 ± 0.03	0.06 ± 0.01	2.34 ± 0.12	SG TT-OSL	79/2000	55 ± 7	MAM-3	76.0 ± 7.4	32.5 ± 3.6
ALV18-5	central-west	SW	ls	212–250	16.8/16.8	0.94 ± 0.05	0.55 ± 0.02	0.06 ± 0.01	1.58 ± 0.09	SG OSL	292/2300	26 ± 2	CAM	52.9 ± 1.1	33.5 ± 2.1
				90–125	16.8/16.8	1.01 ± 0.05	0.55 ± 0.02	0.06 ± 0.01	1.64 ± 0.09	SG TT-OSL	68/2000	54 ± 8	MAM-3	48.8 ± 6.9	29.7 ± 4.5
ALV18-6	central-west	SW	al	212–250	6.6/13.9	1.16 ± 0.06	0.72 ± 0.03	0.06 ± 0.01	1.97 ± 0.10	SG OSL	151/2400	27 ± 3	CAM	71.2 ± 2.1	36.2 ± 2.3
ALV18-7	central-west	SW	al	212–250	5.9/10.8	1.32 ± 0.07	0.89 ± 0.03	0.05 ± 0.01	2.29 ± 0.11	SG OSL	134/2300	28 ± 3	CAM	78.8 ± 2.5	34.4 ± 2.1
				90–125	10.8/10.8	1.41 ± 0.07	0.89 ± 0.03	0.05 ± 0.01	2.38 ± 0.12	SG TT-OSL	53/3800	58 ± 9	MAM-3	87.9 ± 11.3	36.9 ± 5.1
ALV22-4	east	SE	gs	212–250	29.7/29.7	0.44 ± 0.02	0.31 ± 0.01	0.06 ± 0.01	0.84 ± 0.06	SG OSL	196/2200	30 ± 2	CAM	26.4 ± 0.7	31.3 ± 2.4
ALV22-3	east	SE	tc	212–250	15.6/15.6	0.70 ± 0.04	0.32 ± 0.01	0.06 ± 0.01	1.11 ± 0.06	SG OSL	246/1800	24 ± 2	CAM	34.9 ± 0.7	31.3 ± 1.9
ALV22-2	east	SE	tc	212–250	6.5/12.2	0.43 ± 0.02	0.36 ± 0.01	0.06 ± 0.01	0.89 ± 0.04	SG OSL	186/1800	35 ± 3	MAM-3	29.3 ± 0.9	33.0 ± 2.0
ALV22-1	east	SE	bs	212–250	9.0/16.7	1.61 ± 0.08	1.21 ± 0.04	0.06 ± 0.01	2.91 ± 0.16	SG OSL	138/1800	25 ± 3	CAM	99.8 ± 3.0	34.2 ± 2.2

[a] Present-day water content/long-term estimated water content, expressed as % of dry mass of mineral fraction, with an assigned 1σ relative uncertainty of ±20%. The present-day water contents of samples collected from freshly exposed and well-protected deposits (ALV18-4, ALV18-5, ALV22-3, ALV22-4 and ALV22-5) are taken to be representative of long-term moisture conditions. The long-term water contents of all other samples have been estimated as being equivalent to 35% of the present-day saturated water contents for the central-west area (ALV18-1, ALV18-2, ALV18-3, ALV18-6 and ALV18-7) and equivalent to 45% of the present-day saturated water contents for the east area (ALV22-1 and ALV22-2) based on area-specific proportional saturated water contents assessments.

[b] Beta dose rates were calculated using a Risø GM-25-5 low-level beta counter (Bøtter-Jensen and Mejdahl, 1988), after making allowance for beta dose attenuation due to grain-size effects and HF etching (Mejdahl, 1979; Brennan, 2003). Radionuclide concentrations and specific activities of beta counting standards have been converted to dose rates using the conversion factors given in Guérin et al. (2011).

[c] Gamma dose rates were calculated from in situ measurements made at each sample position with a NaI:Tl detector using the 'energy windows' method detailed in Arnold et al. (2012b) and Duval and Arnold (2013). Radionuclide concentrations and specific activities of gamma spectrometry calibration materials, and K, U, Th concentrations determined from the field gamma-ray spectra have been converted to dose rates using the conversion factors given in Guérin et al. (2011).

[d] Cosmic-ray dose rates were calculated according to Prescott and Hutton (1994) and assigned a relative 1σ uncertainty of ±10%.

[e] Total dose rate includes an assumed internal alpha + beta dose rate of 0.03 Gy/ka for quartz, with an assigned relative 1σ uncertainty of ±30%, is based on intrinsic ^{238}U and ^{232}Th contents published by Mejdahl (1987), Bowler et al. (2003), Jacobs et al. (2006), Pawley et al. (2008), and Lewis et al. (2020), and an a-value of 0.04 ± 0.01 (Rees-Jones, 1995; Rees-Jones and Tite, 1997). Intrinsic radionuclide concentrations and specific activities have been converted to dose rates using the conversion factors given in Guérin et al. (2011), making allowance for beta dose attenuation due to grain-size effects (Mejdahl, 1979).

[f] Mean ± total uncertainty (68% confidence interval), calculated as the quadratic sum of the random and systematic uncertainties.
[g] SG OSL = single-grain OSL; SG TT-OSL = single-grain thermally transferred OSL.
[h] Number of D_e measurements that passed the SAR rejection criteria and were used for D_e determination/total number of D_e values analysed.
[i] OD = overdispersion, defined as the relative spread in the De dataset beyond that associated with the measurement uncertainties for individual D_e values.
[j] Age model used to calculate the sample-averaged D_e value for each sample: CAM = central age model; MAM-3 = 3-parameter minimum age model; MAM-4 = 4-parameter minimum age model (Galbraith et al., 1999).
[k] MAM-3 and MAM-4 D_e estimates were calculated after adding, in quadrature, a relative error of 25% to each individual D_e measurement error to approximate the site-specific baseline (best-case scenario) overdispersion observed in well-bleached and unmixed sedimentary samples from this site (i.e. ALV22-1 and ALV22-3). This underlying dose overdispersion value is consistent with average published values of 20 ± 1% and 30 ± 1% reported for well-bleached and unmixed samples by Arnold and Roberts (2009) and Arnold et al. (2022), respectively.
[l] Total uncertainty includes a systematic component of ±2% associated with laboratory beta-source calibration.

Fig. 2. Representative single-grain OSL and TT-OSL D_e distributions for the Lagar Velho dating samples, shown as radial plots. The grey bands on the radial plots are centred on the D_e values used for the age calculations, which were derived using either the central age model (CAM) for the single-grain OSL dataset of ALV18-5 or the 3-parameter minimum age model (MAM-3) for the single-grain OSL and TT-OSL datasets of ALV22-2 and ALV18-3. Individual D_e values that fall within the shaded region are consistent with the MAM-3 or CAM burial doses used for age calculation.

1–4% of TT-OSL D_e measurements per sample are considered suitable for dating purposes after application of the SAR quality assurance criteria (Table S3), with the majority of measured grains (46–76%) being rejected from further consideration because they exhibited weak or no luminescence signal.

Ten of the OSL samples (ALV18-2 to −7; ALV22-1; ALV22-3 to −5) exhibit homogeneous D_e distributions characterised by low dose

dispersion (mean relative D_e range = 2.7), D_e scatter that is reasonably well-represented by the weighted mean value (as indicated by the large proportions of grains lying within the 2σ grey bands), and over-dispersion of 24 ± 2% to 30 ± 2% (Fig. 2a, S4b-h, j-l, Table 2 and Table S4). The overdispersion values for these samples (mean value = 27 ± 1%) are broadly similar to those reported for well-bleached and un-mixed single-grain OSL D_e datasets (e.g., Arnold and Roberts, 2009; Arnold et al., 2022; Hocknull et al., 2020), including those from similar well-bleached depositional settings across the Iberian Peninsula (e.g., Demuro et al., 2019a, 2023; Arnold et al., 2016; Zilhão et al., 2020, 2021b; Rios-Garaizar et al., 2022; Daura et al., 2021). None of the ten D_e datasets are considered significantly positively skewed according to the weighted skewness test outlined by Bailey and Arnold (2006) and Arnold and Roberts (2011) (Table S4). Application of the maximum log likelihood (L_{max}) test (Arnold et al., 2009) indicates that the central age model (CAM) is statistically favoured over the three- or four-parameter minimum age models (MAM-3 or MAM-4) of Galbraith et al. (1999) for all ten D_e datasets (Table S4). Collectively, these single-grain OSL D_e characteristics suggest that the samples do not suffer from major extrinsic D_e scatter related to insufficient bleaching prior to burial (e.g., Arnold et al., 2008, 2011) or widespread post-depositional sediment mixing between units (e.g., Arnold et al., 2012a, 2013). The single-grain OSL ages for these ten samples have therefore been obtained using the weighted mean (CAM) D_e estimate, in accordance with their L_{max} test results (Arnold et al., 2009) (Table 2).

The remaining two OSL samples (ALV18-1 and ALV22-2 from the *us* and *tc* deposits) exhibit more heterogeneous D_e distributions characterised by higher dose dispersion (mean relative D_e range = 4.1), larger proportions of individual D_e values lying outside of the weighted mean burial dose 2σ ranges, overdispersion ranges of 29 ± 1% to 35 ± 3%, and more distinct leading-edges of low D_e values or tails of higher D_e values (Fig. 2b–Fig. S4a, i; Table 2 and Table S4). The single-grain D_e datasets are additionally considered to be significantly positively skewed, and the MAM-3 is statistically favoured over the CAM for both samples (Table S4). These D_e characteristics are consistent with those commonly reported for heterogeneously bleached single-grain OSL

Table 3
Summary of results, data input values and combined U-series and ESR age calculations for samples POR1801A and PR1801B. All uncertainties are quoted at 1σ.

Sample data	POR1801A	POR1801B
Enamel data		
D_e (Gy)[a]	36.5 ± 1.7	32.3 ± 2.3
U (ppm)[b]	0.27 ± 0.07	0.17 ± 0.07
$^{234}U/^{238}U$[c]	0.934 ± 0.021	0.969 ± 0.008[d]
$^{230}Th/^{234}U$[c]	0.485 ± 0.049	0.046 ± 0.003[d]
Alpha Efficiency	0.13 ± 0.02	0.13 ± 0.02
Water content (%)	0	0
Initial enamel thickness (μm)[e]	1443 ± 144	1060 ± 106
Dentine data		
U (ppm)[b]	4.47 ± 0.17	1.67 ± 0.09
$^{234}U/^{238}U$[c]	0.970 ± 0.005	0.969 ± 0.008
$^{230}Th/^{234}U$[c]	0.076 ± 0.002	0.046 ± 0.003
Water (%)	5 ± 3	5 ± 3
Removed enamel thickness (μm)[e]	179 ± 18	130 ± 13
Sediment data		
U (ppm)	3.60 ± 0.43[f]/3.10 ± 0.20[g]	3.60 ± 0.43[f]/3.10 ± 0.20[g]
Th (ppm)	9.75 ± 0.55[f]/8.53 ± 0.49[g]	9.75 ± 0.55[f]/8.53 ± 0.49[g]
K (%)	1.07 ± 0.04[f]/1.00 ± 0.05[g]	1.07 ± 0.04[f]/1.00 ± 0.05[g]
Water (% wet)[h]	10 ± 2	10 ± 2
Removed thickness (μm)[e]	99 ± 10	63 ± 6
Cosmic dose rate (μGy a^{-1})[h]	53 ± 5	53 ± 5
AU/US-ESR age calculations		
Program used	USESR[i]	DATA[j]
Internal dose rate (μGy a^{-1})	33 ± 33	3 ± 1
Beta dose rate, dentine (μGy a^{-1})	1 ± 1	1 ± 0
Beta dose rate, sediment (μGy a^{-1})	128 ± 17	176 ± 18
Gamma + cosmic dose rate (μGy a^{-1})	942 ± 37	942 ± 37
Total dose rate (μGy a^{-1})[k]	1105 ± 92	1122 ± 41
Combined AU/US-ESR age (ka)[l]	33.0 ± 3.2 (AU/US-ESR)	28.7 + 2.3/−2.2 (US-ESR)
EU-ESR age (ka)[m]	32.3 ± 1.9	27.9 ± 2.2

[a] The 1σ D_e uncertainty has been derived by combining the dose response curve fitting uncertainty and the calibration uncertainty for the gamma radiation source (2.3%).
[b] Values obtained from solution U-series analyses.
[c] Values obtained from laser ablation U-series analyses.
[d] Given the unreliable U-series data obtained for the enamel layer using laser ablation analysis (Table S7), the combined U-series/ESR age calculation has been performed using the U-series values obtained from the dentine layer of this particular tooth (see SI text for further explanations).
[e] An assumed relative error of 10% has been assigned to the initial/removed tissue thicknesses.
[f] Dry elemental concentrations obtained using (laboratory) high resolution gamma spectrometry analysis of bulk homogenised sediment. These values were used for the sediment beta dose rate evaluation.
[g] Dry-equivalent elemental concentrations obtained using field gamma spectrometry. These values were used for the gamma dose rate evaluation.
[h] The long-term water content and cosmic dose rate are the same as those obtained for paired luminescence dating sample ALV18-7. Note, the water content for the ESR age calculations is expressed as percentage wet sediment weight, which is the default parameter used in the ESR age calculation programs.
[i] From Shao et al. (2012).
[j] From Grün (2009).
[k] Post-Rn equilibrium has been assumed in the dental tissue and sediment dose rate calculations.
[l] Combined U-series/ESR ages calculated using either the accelerating uptake (AU) model of Shao et al. (2012), and/or the uranium series (US) model of Grün et al. (1988).
[m] EU-ESR age were calculated with DATA program, on the assumption that dental tissues behave as closed-system (EU = Early Uptake model).

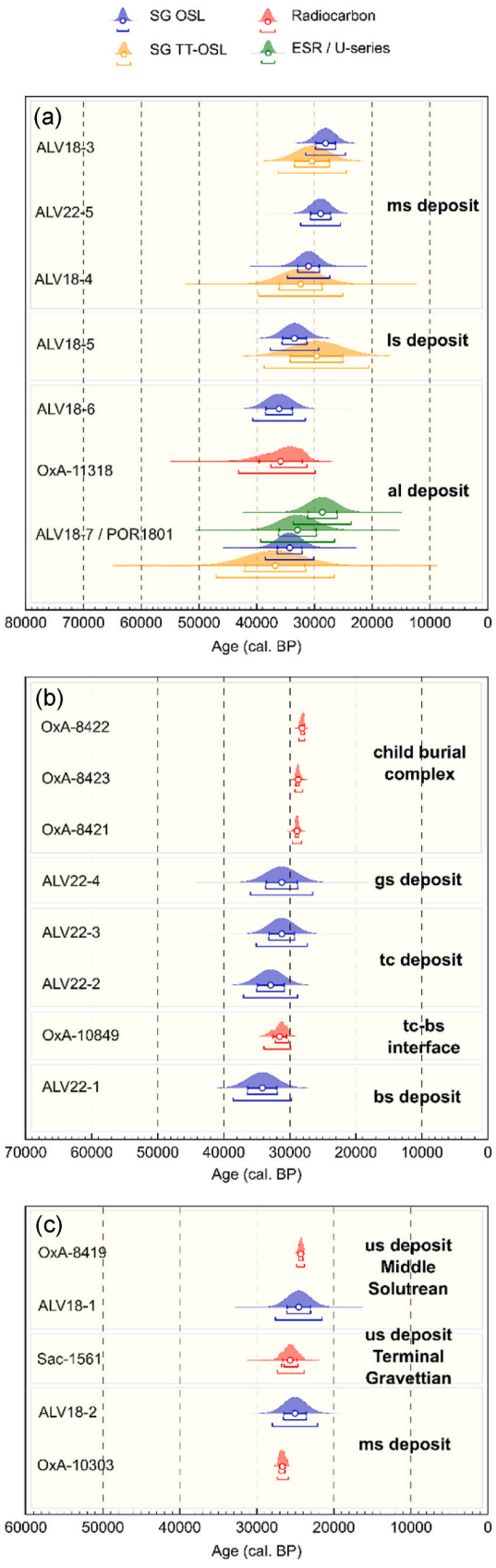

(caption on next column)

Fig. 3. Summary of comparative ages obtained for the geoarchaeological complex (GC) successions in different sectors of the Lagar Velho Rock Shelter. (a) the combined SW and EE sectors spanning the main excavations of the central-west area, (b) the SE sector of the east area, (c) the TP sector (hanging remnant profile) along the backwall recess of the central-west area. The ages obtained for each deposit are represented by different coloured probability distributions. White circles indicate the weighted mean age of each sample, while the horizontal lines beneath each probability distribution denote the 1σ and 2σ uncertainty range (68.3% and 95.4% calibrated age ranges in the case of the ^{14}C samples). The ^{14}C ages have been calibrated using the IntCal20 calibration curve (Reimer et al., 2020) and are expressed in calendar years before AD1950. The original OSL, TT-OSL and combined U-series/ESR ages are also expressed in years before AD1950 so that they are referenced to the same datum as the ^{14}C calibrated ages.

samples (e.g., Olley et al., 1999; Bailey and Arnold, 2006; Arnold et al., 2007), which seems reasonable in this sedimentary context given the host deposits were deposited by slopewash and alluvial processes that could have involved limited transportation distances or localised erosion and entrainment of pre-existing deposits (syn-depositional mixing). Based on these D_e interpretations, we have opted to use the statistically favoured MAM-3 to derive the burial doses for samples ALV18-1 and ALV22-2 (Table 2). However, it is worth noting that the OSL ages obtained for each sample using the MAM-3 and CAM are consistent with each other at 1σ (Table S4); in the case of sample ALV18-3, the ages obtained using the various statistical models differ by only 0.85 ka.

The replicate TT-OSL D_e datasets of samples ALV18-3, ALV18-4, ALV18-5 and ALV18-7 exhibit more pronounced D_e scatter compared to their OSL counterparts (mean relative D_e range = 4.0), as well as significantly higher overdispersion values of 49 ± 6% to 58 ± 9%, enhanced tails of high D_e values, and statistically significant positive skewness at either the 68% or 95% C.I. (Fig. 2c–Fig. S5; Table 2 and Table S4). Additionally, all four datasets are optimally represented by the MAM-3 according to the L_{max} criterion of Arnold et al. (2009) (Table S4). These complex D_e characteristics are interpreted as reflecting the presence, or even dominance, of heterogeneously bleached grain populations, which is consistent with the relatively slow bleaching characteristics of TT-OSL signals (e.g., Demuro et al., 2015; Duval et al., 2017) and the greater potential for insufficient bleaching of residual doses in karst entrance settings that typically experience limited, indirect or filtered daylight exposure (e.g., Demuro et al., 2019a; Arnold et al., 2019).

The combined OSL and TT-OSL ages obtained using the statistically favoured burial dose models (i.e., those selected in accordance with the L_{max} test results) reveal that the central-west area stratigraphic succession (*al* to *us* deposits) spans 36.9 ± 5.1 ka to 24.6 ± 1.5 ka, with the main phase of repeated Late Gravettian occupation (represented by the *ms* and upper *ls* deposits) constrained between 33.5 ± 2.1 ka and 25.1 ± 1.5 ka. The OSL ages obtained for the *bs-tc-gs* succession in the east area span 34.2 ± 2.2 ka 31.3 ± 2.4 ka, providing improved *terminus post quem* constraint on the overlying child burial complex (Table 2).

5. Combined U-series/ESR dating results

Table S5 and Fig. S6 summarise the ESR D_e and dose response curve fitting results for the two enamel samples from Lagar Velho. Given the relatively low natural dose ranges (and thus natural signal intensities) under consideration in this study, it has been necessary to evaluate the sensitivity of the MAAD D_e estimates to different types of dose response curve fitting approaches and net signal calculations. A series of fitting function, data weighting, background-subtraction and baseline subtraction combinations have been considered for this purpose, resulting in five comparative D_e estimates for each sample (D_{e1}-D_{e5}, see Supplementary Information for discussions and Table S5 footnote for definitions). These sensitivity tests reveal that the final burial dose evaluations of POR1801A and POR1801B can be biased by up to 11–13% (D_{e4}/D_{e1}

Table 4
Summary of the single-grain OSL, single-grain TT-OSL, combined U-series/ESR (this study) and ^{14}C ages (Zilhão and Trinkaus, 2002) obtained for the various geoarchaeological complexes (GCs) and depositional events preserved in the central-west and east areas of Lagar Velho Rock Shelter. The provenance details and stratigraphic relationships of the dating samples are shown for each area. The geoarchaeological complexes (GCs) are listed in stratigraphic order from youngest to oldest for each area. Owing to the absence of a continuous longitudinal record of the succession across all sectors, we have not assumed any prior correlative relationships of GCs between the east and central-west areas in the present dating study (with the exception of *tc*, which is preserved in both areas of the site). The ^{14}C samples included in this comparative dating assessment are limited to those that were collected from the same sectors and stratigraphic profiles as the luminescence and U-series/ESR samples, and those that pass our combined ^{14}C sample purity, quality assurance and stratigraphic hygiene criteria (see main text and Table 1 for further details).

Area	GC/event[a]	sector	Single-grain OSL		Single-grain TT-OSL		U-series/ESR		^{14}C		
			Sample	Age ± 1σ (ka)[b]	Sample	Age ± 1σ (ka)[b]	Sample	Age ± 1σ (ka)	Sample	Age ± 1σ (^{14}C yr BP)[c]	Age (cal. BP 95% C.I.)[d]
central-west	us	TP							OxA-8419	20220 ± 180	24823–23841
central-west	us	TP	ALV18-1	24.6 ± 1.5							
central-west	us	TP							Sac-1561	21380 ± 810	27341–23876
central-west	ms	TP	ALV18-2	25.1 ± 1.5							
central-west	ms	TP							OxA-10303	22390 ± 280	27229–26049
central-west	ms	EE	ALV18-3	28.2 ± 1.7	ALV18-3	30.5 ± 3.0					
central-west	ms	EE	ALV22-5	29.0 ± 1.7							
central-west	ms	SW	ALV18-4	31.1 ± 1.8	ALV18-4	32.5 ± 3.6					
central-west	ls	SW	ALV18-5	33.5 ± 2.1	ALV18-5	29.7 ± 4.5					
central-west	tc	SW									
central-west	al	SW							OxA-11318	29800 ± 2500	43132–29869
central-west	al	SW	ALV18-6	36.2 ± 2.3							
central-west	al	SW	ALV18-7	34.4 ± 2.1	ALV18-7	36.9 ± 5.1	POR1801A	33.0 ± 3.2			
central-west	al	SW					POR1801B	$28.7^{+2.3}_{-2.2}$			
east	cb	SE							OxA-8422	23920 ± 220	28640–27727
east	cb	SE							OxA-8423	24520 ± 240	29210–28080
east	cb	SE							OxA-8421	24660 ± 260	29633–28233
east	gs	SE	ALV22-4	31.3 ± 2.4							
east	tc	SE	ALV22-3	31.3 ± 1.9							
east	tc	SE	ALV22-2	33.0 ± 2.0							
east	tc-bs	SE							OxA-10849	27100 ± 900	33915–29834
east	bs	SE	ALV22-1	34.2 ± 2.2							

[a] us = upper slope deposits; ms = intermediate slope deposits; ls = lower slope deposits; tc = transitional complex; al = alluvial complex; cb = child burial complex inset into upper gc deposits; gs = fine gravel and sand deposits; tc–bs = interface between the transitional complex (tc) and lowest slope deposits (bs); bs = lowest slope deposits.

[b] The OSL and TT-OSL ages included in these comparisons have been calculated using the statistically favoured burial dose models (CAM or MAM-3), as determined from the maximum log likelihood (L_{max}) test results (Arnold et al., 2009) (see main text and Table 2 and Table S4 for details).

[c] Conventional uncalibrated ^{14}C age.

[d] Calibrated ^{14}C age presented at 95.4% probability range. Calibration has been undertaken using OxCal 4.4 (Bronk Ramsey, 2009) and IntCal20 (Reimer et al., 2020).

ratios; Table S5) unless appropriate D_{max}–adjusted dose response curve fittings are adopted (following the recommendations of Duval and Grün, 2016) and additional background noise subtractions are incorporated. The combined U-series/ESR ages have therefore been calculated using the D_{e4} values, which take into account these various practical considerations for samples that have low natural dose ranges.

LA U-series analyses performed on a cross-section of each sample yield pseudo-bulk apparent U-series ages of 8.5 ± 0.5 ka and 5.2 ± 0.8 ka for the dentine layers of POR1801A and POR1801B, respectively (2σ uncertainties) (Tables S6–7). These should be regarded as minimum age constraints for the dentine tissues, as U uptake may be significantly delayed after the death of an organism (Grün et al., 2014). The enamel layer LA U-series data yield a much older apparent U-series age of 72.9 ± 21.2 ka for POR1801A (Table S6), most likely indicating a recent uranium leaching overprint (see Supplementary Information for further information). In the case of sample POR1801B, it is not possible to calculate an apparent U-series age for the enamel layer, owing to the trace U concentrations obtained for all LA spots (Table S7). The low U concentrations measured using solution ICP-MS for the enamel layers (<0.5 ppm; Table 3) are close to, or below, the detection limits of the LA analyses, and indicate that the enamel LA data should be treated with caution. Moreover, these low U concentrations reveal that the enamel tissue carries very limited weight in the total dose rate calculation of samples POR1801A and POR1801B, thereby minimising any biases introduced by the choice of uranium uptake modelling (Grün and McDermott, 1994).

The ages obtained by combining the U-series dose rate data and ESR burial dose results are summarised in Table 3. It is not possible to calculate a finite combined U-series/ESR age for sample POR1801A using the uranium series (US) model of Grün et al. (1988) as the enamel tissue has been affected by uranium leaching. However, a finite age of 33.0 ± 3.2 ka can be obtained by applying the accelerating uptake (AU) model of Shao et al. (2012) to the enamel tissue and the US model to the dentine tissue. Interestingly, alternative calculations undertaken using the early uptake (EU), linear uptake (LU) and recent uptake (RU) parametric models all reveal statistically indistinguishable ages for POR1801A (32.3 ± 1.9 ka, 33.3 ± 2.0 ka and 34.3 ± 2.0 ka, respectively). These comparisons confirm that the final age calculation is

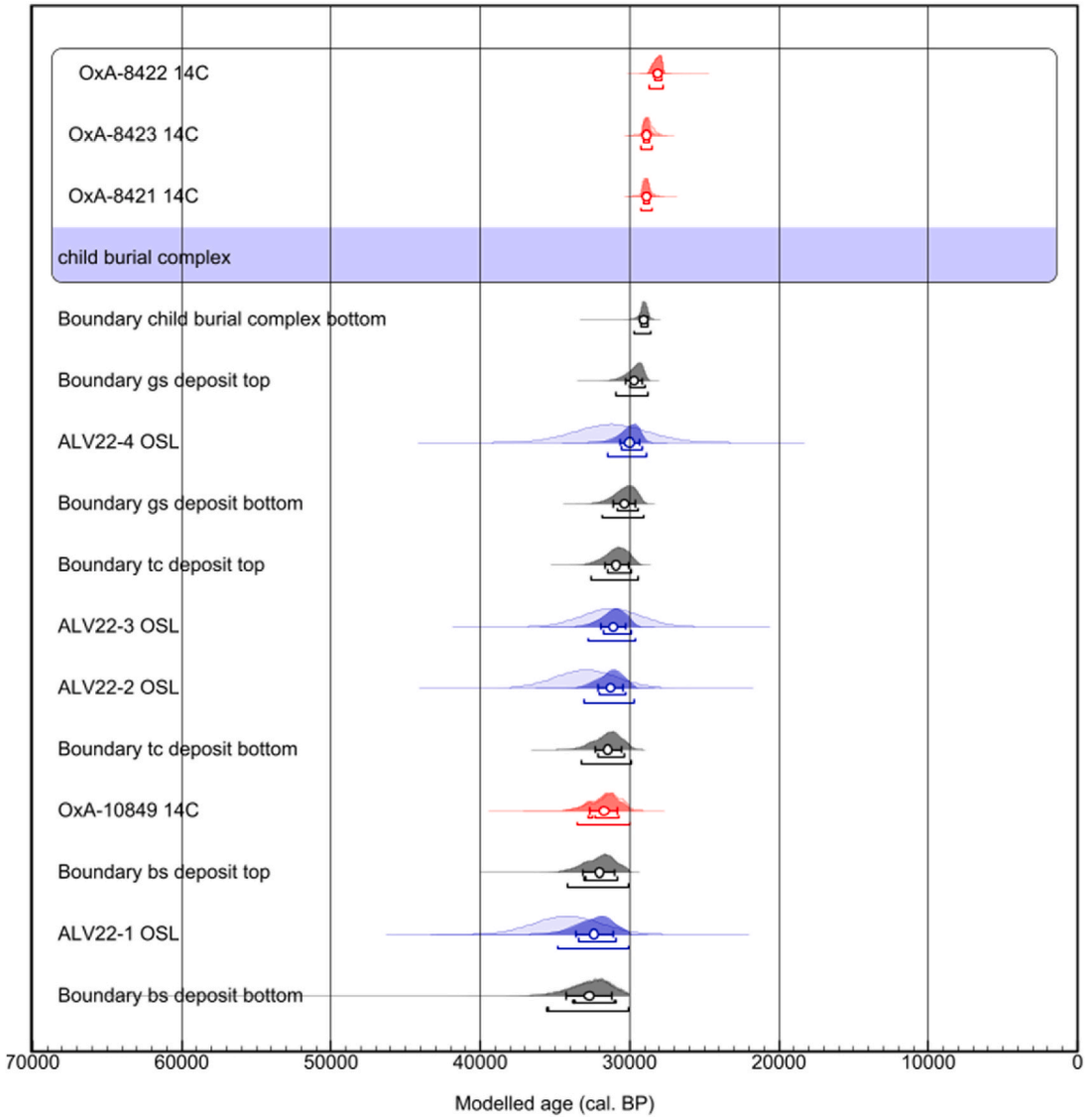

Fig. 4. Bayesian age modelling results for the Lagar Velho east area stratigraphic sequence. The unmodelled age distributions for the OSL and TT-OSL (blue) and ^{14}C (red) dating determinations (likelihoods) are shown as light shaded colour probability distribution functions (PDFs). The modelled posterior distributions for the dating determinations and stratigraphic unit boundaries are shown as dark shaded colour and grey PDFs, respectively. Unmodelled and modelled ages are shown on a calendar year timescale, and both are expressed in years before AD 1950. The white circles and associated error bars represent the mean ages and 1σ uncertainty ranges of the PDFs. The 68.3% and 95.4% ranges of the highest posterior probabilities are indicated by the horizontal bars underneath the PDFs.

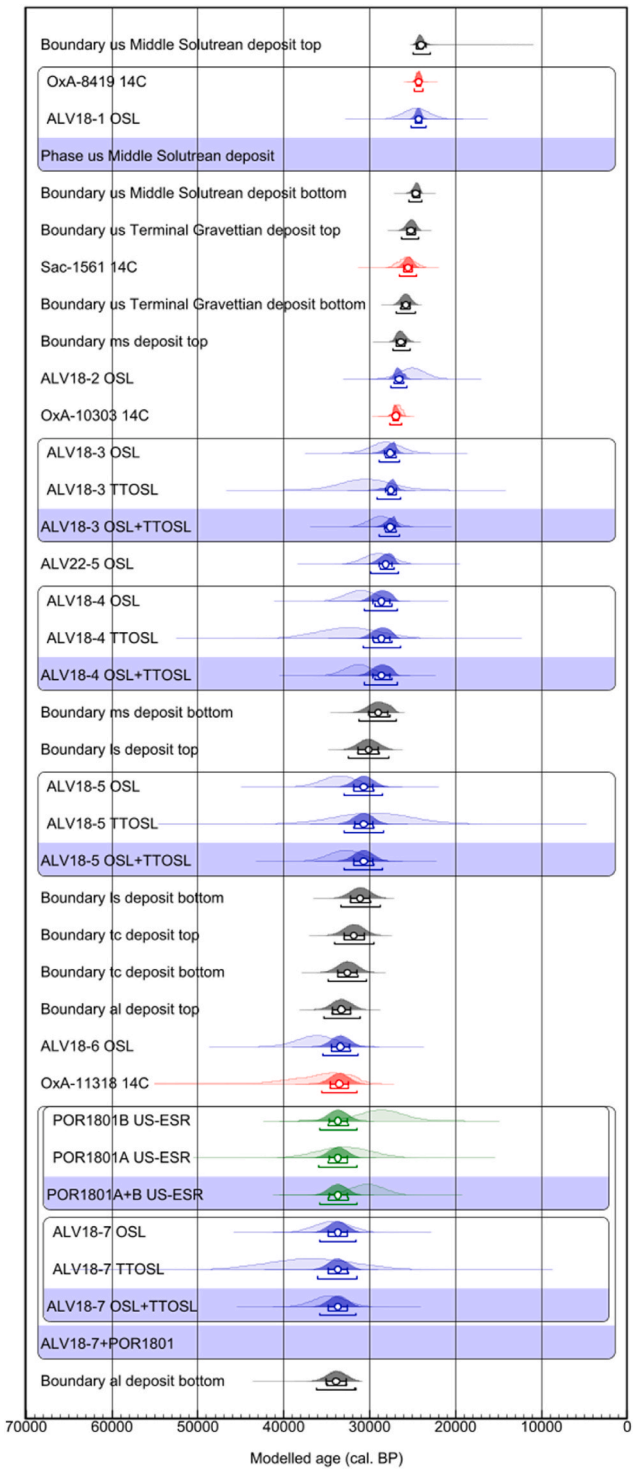

Fig. 5. Bayesian age modelling results for the Lagar Velho central-west area stratigraphic sequence. The unmodelled age distributions for the OSL and TT-OSL (blue), combined U-series/ESR (green) and ^{14}C (red) dating determinations (likelihoods) are shown as light shaded colour probability distribution functions (PDFs). The modelled posterior distributions for the dating determinations and stratigraphic unit boundaries are shown as dark shaded colour and grey PDFs, respectively. Unmodelled and modelled ages are shown on a calendar year timescale, and both are expressed in years before AD 1950. The white circles and associated error bars represent the mean ages and 1σ uncertainty ranges of the PDFs. The 68.3% and 95.4% ranges of the highest posterior probabilities are indicated by the horizontal bars underneath the PDFs.

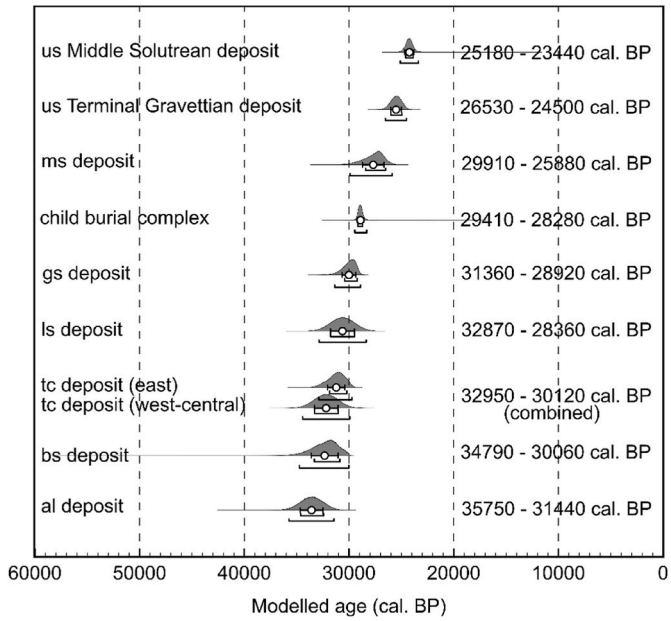

Fig. 6. Bayesian-modelled age distributions for the individual geo-archaeological complexes (GCs) and archaeological complexes preserved in the east and central-west areas of Lagar Velho Rock Shelter. The probability density functions have been calculated from the modelled posterior probabilities of the upper and lower boundaries of each GC or archaeological complex (shown as grey posterior probability distributions in Figs. S9–10) using the *date* query in OxCal v4.4. The white circles and associated error bars represent the mean ages and 1σ uncertainty ranges of the posterior probability distributions. The 68.3% and 95.4% ranges of the highest posterior probabilities are indicated by the horizontal bars underneath the age distributions. The corresponding modelled age ranges shown on the right of the plot represent the 95.4% credible interval probabilities for the age of individual GCs or archaeological complexes (calculated using the *date* query).

largely insensitive to the choice of uranium uptake modelling, reflecting the fact that the total ESR dose rate is dominated by external contributions from the sedimentary environment. The external gamma and beta dose rate components originating from the surrounding sediment account for 80% and 11% of the combined dose rate, whereas the dose rate of the dental tissues (internal and external component from the enamel and dentine, respectively) accounts for <5% of the total dose rate.

In contrast to POR1801A, it is possible to calculate a finite age of $28.7^{+2.3}_{-2.2}$ ka for sample POR1801B using the US model. This highlights the usefulness of undertaking replicate sampling over different regions of individual tooth samples to better evaluate the spatially complex uptake histories of dental tissues. The dose rate of sample POR1801B is similarly dominated by external gamma and beta sediment dose rate contributions (accounting for 95% of the total dose rate), with the dental tissues contributing negligibly to the final age calculation (Table 3). The limited influence of the enamel layer on the total dose rate reinforces our interpretation that the questionable LA U-series ratios obtained for this tissue do not significantly bias the calculated US-ESR age. This is also borne out by the statistically indistinguishable EU-ESR age obtained for POR1801B, which differs from the US-ESR age by < 1 ka (Table 3).

The final AU/US-ESR age of POR1801A and US-ESR age of POR1801B are consistent with each other at 1σ, and they have therefore been combined to derive a mean age of 30.9 ± 2.7 ka for the fossil tooth (1σ uncertainty calculated by multiplying the average relative uncertainties of the replicate ages by the combined average age).

6. Multi-technique dating comparisons

The suitability of the combined single-grain OSL, single-grain TT-

Table 5
Probability matrix showing the relative ordering of Bayesian modelled ages for the various geoarchaeological complexes (GCs) preserved in the east and west-central areas of Lagar Velho Rock Shelter. The ordering probabilities for all paired depositional event permutations have been calculated from the modelled boundary ages of each GC and archaeological complex using the OxCal *order* query (Bronk Ramsey, 2009). The values shown in the matrix represent the probability that the modelled age distribution for a given GC1 (shown vertically in column 1) is younger than that for each of the other GCs at the site (GC2; shown horizontally across row 1). Probabilities >0.95 are taken to indicate a statistically significant chronostratigraphic ordering relationship between GC1 and GC2. Ordering relationships that cannot be differentiated with statistically significant probability (i.e., at >95% C.I.) are taken to indicate potentially coeval GC1 and GC2 modelled age distributions.

P(GC1 < GC2)	GC2								
GC1	*us* Solutrean	*us* Gravettian	*ms*	child burial	*gs*	*ls*	*tc*	*bs*	*al*
***us* Solutrean**	–	0.97	1.00	1.00	1.00	1.00	1.00	1.00	1.00
***us* Gravettian**	0.03	–	0.99	1.00	1.00	1.00	1.00	1.00	1.00
ms	0.00	0.01	–	0.86	0.96	0.97	1.00	1.00	1.00
child burial	0.00	0.00	0.14	–	0.98	0.93	1.00	1.00	1.00
gs	0.00	0.00	0.04	0.02	–	0.68	0.94	0.97	1.00
ls	0.00	0.00	0.03	0.07	0.32	–	0.74	0.85	0.97
tc	0.00	0.00	0.00	0.00	0.06	0.26	–	0.71	0.95
bs	0.00	0.00	0.00	0.00	0.03	0.15	0.29	–	0.77
al	0.00	0.00	0.00	0.00	0.00	0.03	0.05	0.23	–

OSL, AU/US-ESR and quality rated ^{14}C chronological dataset is supported by the stratigraphic consistency of the various ages for the four sectors (Fig. 3), as well as the overlapping replicate ages obtained for individual GCs in a given sampling sector (Table 4, S11). The consistency of the replicate OSL–TT-OSL ages for the SW and EE sectors is noteworthy as not all grains in these samples were seemingly exposed to sufficient daylight to reset their TT-OSL signals (Fig. 3a). Despite this complication, the TT-OSL ages obtained using the statistically favoured age models (MAM-3) are all in agreement with their OSL counterparts at 1σ (Table 4, S11). These comparative results support the applicability of single-grain TT-OSL dating over Late Pleistocene timescales in some relatively complex sedimentary contexts, as long as appropriate statistical age models are considered. Similarly, the broad agreement between the replicate AU/US-ESR (30.9 ± 2.7 ka) and luminescence ages (34.4 ± 2.1 ka to 36.2 ± 2.3 ka) for the SW sector *al* deposits (Fig. 3a) supports the inclusion of D_{max}–adjusted dose response curve fitting and background/baseline subtracted signal integration for these relatively young fossil samples. The consistency of the luminescence and AU/US-ESR ages also implies that the deer mandible fossil and the host *al* deposits are coeval (i.e., the fossil has not been reworked from significantly older deposits found elsewhere in the area).

We cannot exclude the possibility that the minor difference in the mean luminescence and AU/US-ESR ages (~3.5–5.3 ka) may have arisen, at least in part, from the difficulties of capturing the true gamma dose rate contributions of the fossil mandible in our dosimetric evaluations for enamel sample POR1801 A/B. The relative gamma dose rate contribution of the immediately surrounding fossil material (adjacent teeth and bone) is assumed to have been minimal given the limited size of the mandible fragment (Fig. S6a) and the fact that the U concentration of the mandibular materials are not significantly different from the U concentration measured for the host sediment using *in situ* field gamma spectrometry (Table 3). The latter is supported by the U concentration data obtained for the POR1801 A/B dentine fractions, a material of similar composition to the bone and reflecting the tooth material surrounding the enamel dating samples. The dentine fractions have an average U concentration of 3.1 ppm (ranging from 1.7 to 4.5 ppm), i.e. consistent with the U concentration measured for the surrounding sediment matrix using field gamma spectrometry (3.6 ± 0.4 ppm; Table 3). However, it is also worth considering that U uptake may be significantly delayed after the death of an organism (Grün et al., 2014) and that fossil bones typically contain insignificant Th and K concentrations compared to host sediment matrices (Grün, 1989). Both of these factors may have contributed to minor differences in the time-averaged gamma dose rate contributions of the fossil mandible and the host sediment deposits, and may mean that the gamma dose rate measured for the host sediment using *in situ* field gamma spectrometry may slightly overestimate the true long-term gamma dose rate experienced by fossil sample POR1801. To confirm the suitability of our dose rate assumptions and further examine any potential spatial or time-averaged biases, it would be worth undertaking a more comprehensive evaluation of the mandible gamma dose rate contribution in future studies using Monte Carlo dosimetry simulation software such as DosiVox (Martin et al., 2015) in conjunction with more detailed U-series/ESR dose rate evaluations.

The eight paired single-grain OSL–(semi-)independent age estimates are well-represented by a weighted linear regression function (R^2 = 0.78) that is consistent with the 1:1 slope at 2σ (Fig. S9). The intercept of the weighted linear function also overlaps with unity, though this fitting parameter has a relatively large uncertainty as the combined dataset covers a limited age range. Importantly, the *p*-value of the correlation coefficient is 0.004, indicating statistically significant linear correspondence between the paired single-grain OSL–(semi-)independent ages at the >99% C.I. (Fig. S9).

A X^2 homogeneity test (Galbraith, 2003) was used to formally test whether the paired OSL–(semi-)independent ages of individual samples are consistent with a shared value at their 1σ and 2σ ranges. This test reveals that all eight paired OSL–TT-OSL, OSL–combined TT-OSL/U-series/ESR and OSL–^{14}C ages agree with a common value at the 95.4% C.I. (Table S12). Application of a one-sample Student's *t*-test confirms that the paired OSL–(semi-)independent age datasets do not exhibit any statistically significant differences at the 95.4% C.I. (Table S12). In sum, multiple statistical evaluations support the reliability of the paired ages and the combined comparative datasets obtained in this study, providing confidence in the new multi-technique chronological framework established at Lagar Velho.

7. Bayesian chronostratigraphy

The stratigraphic consistency of the chronological datasets is further borne out by the suitability of the Bayesian modelling results for the east and central-west areas of Lagar Velho Rock Shelter (Figs. 4 and 5; Tables S9–10; see discussions of modelling convergence integrals and absence of statistical outliers in the Supplementary Information). The modelled ages of individual GCs and archaeological complexes (calculated from the modelled posterior probabilities of the upper and lower boundaries of each depositional event using the OxCal *date* query) reveal that the east area sedimentary succession spans 34,790 cal. BP to 28,280 cal. BP (all modelled ages quoted herein represent the 95.4% credible intervals) (Fig. 6; Table S9). The modelling results for the central-west area succession reveals a similar basal age beginning at 35,750 cal. BP, with discontinuous sedimentation continuing until 23,440 cal. BP (Fig. 6; Table S10). The combined modelled age ranges for the lowest

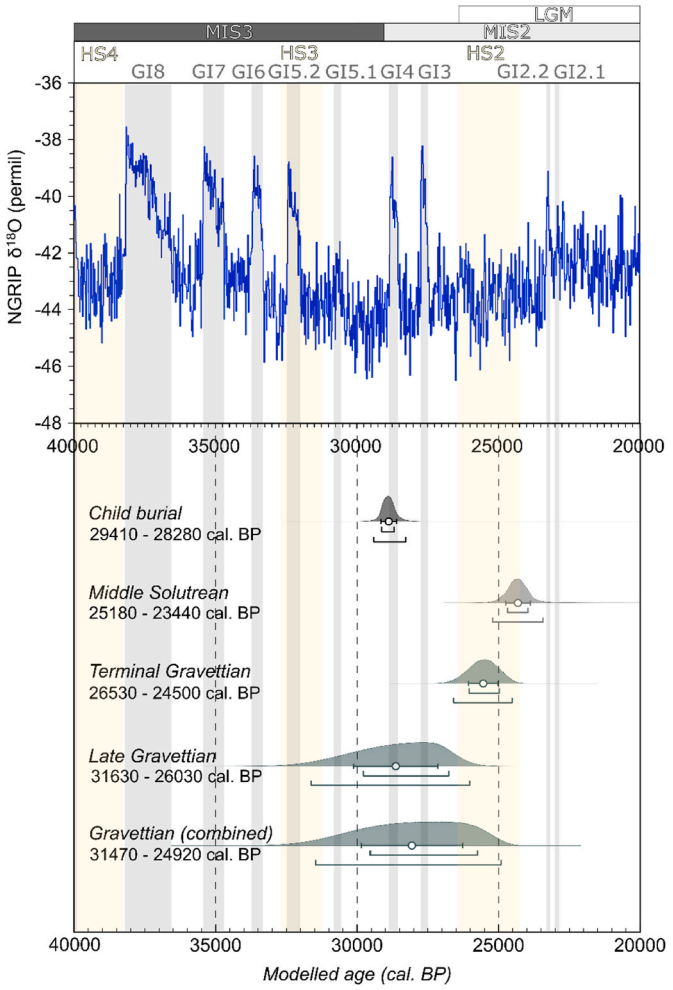

Fig. 7. Bayesian modelled age ranges for Upper Palaeolithic human activity at Lagar Velho, shown against the Greenland Ice Core Chronology 2005 (GICC05) $\delta^{18}O$ temperature record (Rasmussen et al., 2014) (with original GICC05 b2k timescale converted to cal. BP to enable direct comparisons with our modelled age probability distributions). The timing of Greenland Interstadials (GI) 2.1 to 8 are shown as vertical grey shaded bands (Rasmussen et al., 2014). The timing of Heinrich Stadials (HS) 2 to 4 are shown as vertical yellow shaded bands (Sánchez Goñi and Harrison, 2010). The Marine Isotope Stage (MIS) boundary ages correspond to those derived from the globally distributed benthic stack $\delta^{18}O$ records of Lisiecki and Raymo (2005). The Last Glacial Maximum (LGM) age range (*sensu lato*) is based on global sea level low-stand assessments of Clark et al. (2009). The probability distribution functions have been calculated from the modelled posterior probabilities of the upper and lower boundaries of individual geoarchaeological complexes (GCs) or grouped GCs that contain similar cultural complexes using the *date* query in OxCal v4.4. The white circles and associated error bars represent the mean ages and 1σ uncertainty ranges of the posterior probability distributions. The 68.3% and 95.4% ranges of the highest posterior probabilities are indicated by the horizontal bars underneath the age distributions. The corresponding modelled age ranges shown on the left of the plot represent the 95.4% credible interval probabilities for individual GCs or grouped GCs that contain similar cultural complexes (calculated using the *date* query).

GCs (*al* and *bs*) reveal that alluvial deposition dominated in the central-west area prior to 31,440 cal. BP and brecciated slopewash accumulations dominated in the east area prior to 30,060 cal. BP. The stratigraphic successions in both areas record temporally overlapping transitions to alternating gravity-derived sediments and alluvial input (*tc*) between 32,950 and 30,120 cal. BP, though the timing of the *tc* deposits in the central-west area model is currently only indirectly constrained from the assigned GC stratigraphic ordering relationships and bracketing ages on surrounding deposits. The combined ages for the uppermost GCs (*gs*, *ls*, *ms*, *us*) reveal slopewash and gravity-driven accumulations dominated in both the east and central-west areas from 32,870 to 28,360 cal. BP onwards. The age of the child burial complex, which is inset into the upper part of the *gs* deposit in the east area, is refined to 29,410–28,280 cal. BP (Fig. 6; Tables S9–10).

Application of the OxCal *difference* query (Bronk Ramsey, 2009) to the posterior boundary age ranges of each modelled depositional event reveals an absence of any single statistically significant temporal hiatuses between successive GCs in the depositional sequences. A potential sedimentary hiatus between the *ls* and *ms* deposits has been suggested in the SC sector (not studied here) based on evidence for a weakly developed A soil horizon in the uppermost *ls* layers (Zilhão and Trinkaus, 2002). However, the modelling results for the central-west area imply that this period of soil development was relatively short-lived in comparison to the size of the existing dating uncertainties. Additional ^{14}C and OSL sample collection may be useful for further refining the temporal dynamics of the *ls-ms* interface.

The modelled ages for individual depositional events were examined using the *order* query (Bronk Ramsey, 2009) to investigate the chronological relationships of the various GCs preserved in the east and west-central areas. The matrix of relative ordering for all paired depositional event permutations (Table 5) shows that statistically significant ordering relationships can be ascertained for most of the GCs across the two areas (i.e., those permutations in Table 5 with ordering probability assessments >95%). However, there are two notable exceptions. First, the *bs* deposits in the east area and the *al* deposits in the central-west area are considered pene-contemporaneous according to their order probabilities (i.e., *bs* v *al* ordering cannot be differentiated with statistically significant probability >95%; Table 5). The lack of clear ordering supports the interpretation that the *bs* and *al* deposits could represent heteropic equivalents of each other related to lateral variations in subaerial and alluvial deposition (Zilhão and Trinkaus, 2002). Second, the ordering of the *ms* and *ls* deposits in the central-west area, and the *gs* deposits and the child burial complex in the east, cannot be fully differentiated with >95% probability (Table 5). Consequently, the child burial complex and the broader Gravettian archaeological sequence may be considered as temporally overlapping based on current dating evidence. However, it is worth emphasising that the child burial took place over a much shorter period (hours or days) than the more protracted and recurrent *ls–ms* Gravettian occupations, hence these two events should not be interpreted as occurring simultaneously over the full duration of the modelled age ranges. Interestingly, the marginal ordering probabilities suggest a potential age succession of *ls* > *gs* > *child* > *ms* (Table S5 Fig. 6), though further stratigraphic analysis and correlations are imperative for establishing more definitive ordering relationships between these events. Additionally, there are some uncertainties in the ordering assessments of *tc* vis à vis *gs*, *ls* and *bs*, which largely reflect the absence of direct dating on *tc* deposits in the central-west area. Regardless, the chronostratigraphic relationships of *tc* can be directly constrained as *tc* > *ls* and *gs* < *tc* < *bs* from the sedimentary profiles preserved in the SE and SW sectors (Zilhão and Trinkaus, 2002; Fig. S1).

8. Discussion – upper Palaeolithic occupation dynamics of Lagar Velho

The new chronological assessments of Lagar Velho enable us to place the human occupation sequence in a firmer regional climatic and archaeological context (Fig. 7). The Bayesian modelled ages for the various episodes of Upper Palaeolithic human activity span 31.6–23.4 ka cal. BP (calculated by applying the *date* query to the modelled upper and lower boundary distributions of individual GCs or grouped GCs with shared cultural associations). The Lagar Velho archaeological and palaeoanthropological record therefore covers a significant period of global environmental and cultural change taking place within the last glacial cycle, particularly the transition from the more favourable

(though relatively cool) conditions of Marine Isotope Stage (MIS) 3 to the colder and drier conditions of MIS 2 at ~29 ka (Lisiecki and Raymo, 2005), and including the pronounced climatic downturn that affected much of the Iberian Peninsula ~26 ka (e.g., Domínguez-Villar et al., 2015; Wolf et al., 2021) at the onset of the Last Glacial Maximum (LGM) (26.5–19.0 ka *sensu lato;* Clark et al., 2009). This longer term climatic deterioration was also punctuated by a series of dramatic, shorter term climate fluctuations associated with abrupt warming and subsequent cooling cycles in Greenland (Dansgaard–Oeschger cycles; comprising Greenland Interstadials, GI, and Greenland Stadials, GS; Rasmussen et al., 2014), including several distinct cold periods associated with ice-rafted debris formation in the North Atlantic (Heinrich Stadials) (Sánchez Goñi and Harrison, 2010).

The timing of the Late Gravettian, Terminal Gravettian (equivalently termed the Proto-Solutrean in some contexts; Straus, 2015) and Middle Solutrean techno-complex succession at Lagar Velho correlates with both long- and short-term climate trends, as shown in Fig. 7. Specifically, the Late Gravettian occupation (spanning the *ms* and uppermost *ls* deposits) began 31.6 ka cal. BP, coinciding with the end of HS3 (31.3 ka cal. BP), and continued until the emergence of HS2 at 26.0 ka cal. BP. The child burial complex is chronologically aligned with the Late Gravettian occupation phase between 29.4 and 28.3 ka cal. BP, which corresponds to the MIS 3/2 transition and potentially occurred within the GI4 climatic amelioration. The modelled age of 26.5–24.5 ka cal. BP for the Terminal Gravettian or Proto-Solutrean (*us* deposit) falls exclusively within HS2 (26.5–24.3 ka cal. BP) towards the beginning of the LGM, while the Middle Solutrean occupation at 25.2–23.4 ka (*us* deposit) also overlaps with HS2 and extends almost to the end of GS3 (23.3 ka) within the LGM. The emergent material cultures associated with HS2 are particularly noteworthy as they are aligned with widespread cold and arid conditions across Iberia (e.g., Cacho et al., 2001; Vegas et al., 2010; Domínguez-Villar et al., 2013; González-Sampériz et al., 2020; Pérez-Díaz and López-Sáez, 2021). In sum, the combined Gravettian occupation (including the Terminal Gravettian or Proto-Solutrean) spans four GI/GS periods and two HS cycles, supporting the ecological adaptability of populations in the Estremadura region of Portugal during the contrasting climate regimes of late MIS 3 and early MIS 2.

The age ranges obtained for the various Upper Palaeolithic techno-complexes at Lagar Velho are consistent with those obtained elsewhere in Southern Iberia and therefore reinforce current knowledge of regional occupation dynamics. A recent Bayesian modelling synthesis study of Gravettian sites from the Estremadura, Algarve and Côa Valley regions of Portugal, for instance, reveals that the Gravettian–Proto-Solutrean boundary occurred between 27.4 and 26.3 ka cal. BP (Bicho et al., 2015), in broad agreement with the Late Gravettian occupation termination age of 26.0 ka cal. BP obtained at Lagar Velho. Cascalheira and Bicho (2013) argued that the Proto-Solutrean of central and southern Portugal spanned 27.0–24.0 ka cal. BP from a review of fourteen sites, which is consistent with our revised Terminal Gravettian age of 26.5–24.5 ka cal. BP for Lagar Velho. A meta-analysis modelled age of 25.5–24.2 ka cal. BP has also been obtained for the Middle Solutrean occupations of southern Iberia (Cascalheira and Bicho, 2015), overlapping with the updated Middle Solutrean age of 25.2–23.4 ka at Lagar Velho.

Our latest dating results for Lagar Velho, combined with the published chronological syntheses of regional occupations, highlight the significance of central and southern Portugal as refugia for Upper Palaeolithic populations during the LGM when much of northern and central Europe was experiencing extreme cold, aridity and expanded glacial coverage (Straus, 2015, 2018). Intriguingly, the concentration of Solutrean populations around the Estremadura region of central-western Portugal during HS2 coincides with the recently documented Peña Capón human occupation sequence spanning 26.1–23.8 ka cal. BP in the central Iberian interior (Alcaraz-Castaño et al., 2021); a region that was traditionally thought to have been inhospitably arid, with pronounced loess deposition during HS2 (Wolf et al., 2018, 2021). The broadly contemporaneous occupation histories of these two regions are reinforced by evidence for shared provenance of lithic raw materials between several Côa Valley and northern Meseta sites (e.g. Aubry et al., 2012; 2015). These findings suggest that central Portugal – with its favourable climate, abundant coastal resources, widespread sheltered karstic environments, and well-connected, natural migratory corridors (particularly the Tagus Basin) – is of key significance not only for understanding the long-term survival of European human populations during the extremes of MIS 2, but also for providing insights into the broader connectivity of populations across the Iberian Peninsula during the LGM.

9. Conclusion

Our chronological evaluation of Lagar Velho Rock Shelter demonstrates the usefulness of undertaking multi-technique dating comparisons that target complementary dating materials, and the worth of including sample purity and quality assurance assessments for published ^{14}C datasets. Stratigraphically consistent ages ($n = 26$) are obtained for the archaeological infill sequence using four different dating methods, providing a robust interpretive framework and underscoring the significant role that single-grain OSL and combined U-series/ESR dating can play in refining early Upper Palaeolithic histories of Iberia. The Lagar Velho sediment bleaching characteristics are generally well-suited for OSL dating. Single-grain TT-OSL and combined U-series/ESR dating are both applicable over Late Pleistocene timescales at this site when adopting appropriate age model selection, net signal integration and dose-response curve fitting procedures. Standard ABA ^{14}C pre-treatment appears suitable for removing contaminants from the subset of bone and charcoal samples that pass minimum analytical quality criteria.

Bayesian modelling of the combined chronological dataset reveals a site accumulation history spanning a duration of at least 12.3 ka and provides improved age constraints on all GCs; particularly the *al*, *bs*, *tc*, *gs* and *ls* deposits that were previously undated or imprecisely constrained. Comparison of the modelled GC ages in the east and west-central areas enables improved temporal correlation of depositional events across stratigraphically disconnected sectors of the site. This analysis reveals that the child burial complex and the Late Gravettian archaeological sequence can be ascribed to an overlapping time period based on current dating evidence, albeit they represent events of different duration.

The new dating assessments confirm the chronological significance of Lagar Velho for assessing early Upper Palaeolithic cultural transitions in Iberia. The site records three periods of human activity during contrasting climate regimes of late MIS 3 and early MIS2: namely, the Late Gravettian 31.6–26.0 ka, the Terminal Gravettian 26.5–24.5 ka, and the Middle Solutrean 25.2–23.4 ka. The timing of these occupations, and their apparent correspondence with short- and long-term climate cycles, underscores the ecological and cultural adaptability of local populations, and highlights the significance of central western Portugal for supporting regional human populations during HS2 and the broader LGM.

CRediT authorship contribution statement

L.J. Arnold: Conceptualization, Data curation, Formal analysis, Funding acquisition, Investigation, Methodology, Project administration, Resources, Validation, Visualization, Writing – original draft, Writing – review & editing. **M. Demuro:** Conceptualization, Data curation, Formal analysis, Funding acquisition, Investigation, Methodology, Project administration, Resources, Validation, Visualization, Writing – original draft, Writing – review & editing. **M. Duval:** Formal analysis, Investigation, Methodology, Resources, Validation, Writing – original draft, Writing – review & editing. **R. Grün:** Formal analysis, Investigation, Methodology, Writing – review & editing. **M. Sanz:** Conceptualization, Funding acquisition, Investigation, Project

administration, Resources, Writing – review & editing. **A.M. Costa:** Conceptualization, Funding acquisition, Investigation, Project administration, Resources, Writing – review & editing. **A.C. Araújo:** Conceptualization, Funding acquisition, Investigation, Project administration, Resources, Writing – review & editing. **J. Daura:** Conceptualization, Funding acquisition, Investigation, Project administration, Resources, Writing – review & editing.

Declaration of competing interest

The authors declare the following financial interests/personal relationships which may be considered as potential competing interests: Martina Demuro reports financial support was provided by Australian Research Council. Mathieu Duval reports financial support was provided by Spanish ministry for Science and Innovation. Montserrat Sanz reports financial support was provided by Spanish ministry for Science and Innovation. Joan Daura reports financial support was provided by Portuguese Directorate-General for Cultural Heritage. Joan Daura reports financial support was provided by Spanish Ministry for Culture and Sport. Joan Daura reports financial support was provided by Government of Catalonia. If there are other authors, they declare that they have no known competing financial interests or personal relationships that could have appeared to influence the work reported in this paper.

Data availability

Data will be made available on request.

Acknowledgements

Financial support for this research was provided by Australian research Council (ARC) Future Fellowship Project FT200100816 and Discovery Early Career Researcher Award DE160100743 awarded to M. Demuro, as well as Spanish Ministry for Science and Innovation Ramón y Cajal Postdoctoral Grants RYC2021-032999-I and RYC2018-025221-I, awarded to M. Sanz and M. Duval, respectively. Grant RYC2018-025221-I is funded by MCIN/AEI/10.13039/501100011033 and by 'ESF Investing in your future'. Additional research support was provided by Portuguese Directorate-General for Cultural Heritage grant ALV2018, Spanish Ministry for Science and Innovation grants PID2020-113960 GB-100 and PID2021-123092NB-C22, Spanish Ministry for Culture and Sport grant T002020N0000045536, and Catalan Government project SGR2021-00337. Grant PID2021-123092NB-C22 is funded by MCIN/AEI/10.13039/501100011033 and 'ERDF A way of making Europe'. The excavations at Lagar Velho Rock Shelter were undertaken with financial and technical assistance from the Leiria Municipality and Museum, for which we particularly thank Vânia Carvalho, and from CIBIO–InBIO-BIOPOLIS. We are also grateful to Gilian Ross and Rhianna Power (University of Adelaide) for their assistance with preparing and measuring the optical dating samples, and María Jesús Alonso Escarza (CENIEH) for technical support with the U-series/ESR analytical procedures.

Appendix A. Supplementary data

Supplementary data to this article can be found online at https://doi.org/10.1016/j.quageo.2024.101572.

References

Alcaraz-Castaño, M., Alcolea-González, J.J., de Andrés-Herrero, M., Castillo-Jiménez, S., Cuartero, F., Cuenca-Bescós, G., Kehl, M., López-Sáez, J.A., Luque, L., Pérez-Díaz, S., Piqué, R., Ruiz-Alonso, M., Weniger, G.-C., Yravedra, J., 2021. First modern human settlement recorded in the Iberian hinterland occurred during Heinrich Stadial 2 within harsh environmental conditions. Sci. Rep. 11, 15161.

Almeida, F., Moreno-García, M., Angelucci, D.E., 2009. From under the bulldozer's claws: the EE15 Late Gravettian occupation surface of the Lagar Velho rock-shelter. World Archaeol. 41, 242–261.

Ambrose, S.H., 1990. Preparation and characterisation of bone and tooth collagen for isotopic analysis. J. Archaeol. Sci. 17, 431–451.

Arnold, L.J., Roberts, R.G., 2009. Stochastic modelling of multi-grain equivalent dose (De) distributions: implications for OSL dating of sediment mixtures. Quat. Geochronol. 4, 204–230.

Arnold, L.J., Roberts, R.G., 2011. Paper I – optically Stimulated Luminescence (OSL) dating of perennially-frozen deposits in north-central Siberia: OSL characteristics of quartz grains and methodological considerations regarding their suitability for dating. Boreas 40, 389–416.

Arnold, L.J., Bailey, R.M., Tucker, G.E., 2007. Statistical treatment of fluvial dose distributions from southern Colorado arroyo deposits. Quat. Geochronol. 2, 162–167.

Arnold, L.J., Roberts, R.G., Macphee, R.D.E., Willerslev, E., Tikhonov, A.N., Brock, F., 2008. Optical dating of perennially frozen deposits associated with preserved ancient plant and animal DNA in north-central Siberia. Quat. Geochronol. 3, 114–136.

Arnold, L.J., Roberts, R.G., Galbraith, R.F., DeLong, S.B., 2009. A revised burial dose estimation procedure for optical dating of young and modern-age sediments. Quat. Geochronol. 4, 306–325.

Arnold, L.J., Roberts, R.G., MacPhee, R.D.E., Haile, J.S., Brock, F., Möller, P., Froese, D. G., Tikhonov, A.N., Chivas, A.R., Gilbert, M.T.P., Willerslev, E., 2011. Paper II – dirt, dates and DNA: OSL and radiocarbon chronologies of perennially-frozen sediments and their implications for sedimentary ancient DNA studies. Boreas 40, 417–445.

Arnold, L.J., Demuro, M., Navazo Ruiz, M., 2012a. Empirical insights into multi-grain averaging effects from 'pseudo' single-grain OSL measurements. Radiat. Meas. 47, 652–658.

Arnold, L.J., Duval, M., Falguères, C., Bahain, J.J., Demuro, M., 2012b. Portable gamma spectrometry with cerium-doped lanthanum bromide scintillators: suitability assessments for luminescence and electron spin resonance dating applications. Radiat. Meas. 47, 6–18.

Arnold, L.J., Demuro, M., Navazo, M., Benito-Calvo, A., Pérez-González, A., 2013. OSL dating of the Middle Palaeolithic Hotel California site, Sierra de Atapuerca, north-central Spain. Boreas 42, 285–305.

Arnold, L.J., Demuro, M., Parés, J.M., Arsuaga, J.L., Aranburu, A., Bermúdez de Castro, J.M., Carbonell, E., 2014. Luminescence dating and palaeomagnetic age constraint on hominins from Sima de los Huesos, Atapuerca, Spain. J. Hum. Evol. 67, 85–107.

Arnold, L.J., Demuro, M., Parés, J.M., Pérez-González, A., Arsuaga, J.L., Bermúdez de Castro, J.M., Carbonell, E., 2015. Evaluating the suitability of extended-range luminescence dating techniques over early and Middle Pleistocene timescales: published datasets and case studies from Atapuerca, Spain. Quat. Int. 389, 167–190.

Arnold, L.J., Duval, M., Demuro, M., Spooner, N.A., Santonja, M., Pérez-González, A., 2016. OSL dating of individual quartz 'supergrains' from the Ancient Middle Palaeolithic site of Cuesta de la Bajada, Spain. Quat. Geochronol. 36, 78–101.

Arnold, L.J., Demuro, M., Spooner, N.A., Prideaux, G.J., McDowell, M.C., Camens, A.B., Reed, E.H., Parés, J.M., Arsuaga, J.L., Bermúdez de Castro, J.M., Carbonell, E., 2019. Single-grain TT-OSL bleaching characteristics: insights from modern analogues and OSL dating comparisons. Quat. Geochronol. 49, 45–51.

Arnold, L.J., Demuro, M., Power, R. Priya, Duval, M., Guilarte, V., Weij, R., Woodhead, J., White, L., Bourne, S., Reed, E.H., 2022. Examining sediment infill dynamics at Naracoorte Cave megafauna sites using multiple luminescence dating signals. Quat. Geochronol. 70, 101301.

Aubry, T., Luís, L., Dimuccio, L.A., 2012. Nature vs. Culture: present-day spatial distribution and preservation of open-air rock art in the Côa and Douro River Valleys (Portugal). J. Archaeol. Sci. 39, 848–866.

Aubry, T., Luis, L., Mangado Llach, J., Matias, H., 2015. Adaptation to resources and environments during the last glacial maximum by hunter-gatherer societies in Atlantic Europe. J. Anthropol. Res. 71, 521–544.

Bailey, R.M., Arnold, L.J., 2006. Statistical modelling of single grain quartz De distributions and an assessment of procedures for estimating burial dose. Quat. Sci. Rev. 25, 2475–2502.

Bicho, N., Marreiros, J., Cascalheira, J., Pereira, T., Haws, J., 2015. Bayesian modeling and the chronology of the Portuguese Gravettian. Quat. Int. 359–360, 499–509.

Bird, M.I., Ayliffe, L.K., Fifield, L.K., Turney, C.S.M., Cresswell, R.G., Barrows, T.T., David, B., 1999. Radiocarbon dating of 'old' charcoal using a wet oxidation, stepped-combustion procedure. Radiocarbon 41, 127–140.

Bøtter-Jensen, L., Mejdahl, M., 1988. Assessment of beta dose-rate using a GM multicounter system. Nucl. Tracks Radiat. Meas. 14, 187–191.

Bowler, J.M., Johnston, H., Olley, J.M., Prescott, J.R., Roberts, R.G., Shawcross, W., Spooner, N.A., 2003. New ages for human occupation and climate change at Lake Mungo, Australia. Nature 421, 837–840.

Braadbaart, F., Poole, I., 2008. Morphological, chemical and physical changes during charcoalification of wood and its relevance to archaeological contexts. J. Archaeol. Sci. 35, 2434–2445.

Braadbaart, F., Poole, I., van Brussel, A.A., 2009. Preservation potential of charcoal in alkaline environments: an experimental approach and implications for the archaeological record. J. Archaeol. Sci. 36, 1672–1679.

Brennan, B.J., 2003. Beta doses to spherical grains. Radiat. Meas. 37, 299–303.

Brock, F., Bronk Ramsey, C., Higham, T.F.G., 2007. Quality Assurance of ultrafiltered bone dating. Radiocarbon 49, 187–192.

Bronk Ramsey, B.C., 2009. Bayesian analysis of radiocarbon dates. Radiocarbon 51, 337–360.

Cacho, I., Grimalt, J.O., Canals, M., Sbaffi, L., Shackleton, N.J., Schönfeld, J., Zahn, R., 2001. Variability of the western Mediterranean Sea surface temperature during the last 25,000 years and its connection with the Northern Hemisphere climatic changes. Paleoceanogr. Paleoclimatol. 16, 40–52.
Cascalheira, J., Bicho, N., 2013. Hunter-gatherer ecodynamics and the impact of the Heinrich Event 2 in central and southern Portugal. Quat. Int. 318, 117–127.
Cascalheira, J., Bicho, N., 2015. On the chronological structure of the Solutrean in southern Iberia. PLoS One 10, e0137308.
Clark, P.U., Dyke, A.S., Shakun, J.D., Carlson, A.E., Clark, J., Wohlfarth, B., Mitrovica, J. X., Hostetler, S.W., McCabe, A.M., 2009. The last glacial maximum. Science 325, 710–714.
Daura, J., Sanz, M., Demuro, M., Arnold, L.J., Costa, A.M., Moreno, J., da Conceição Freitas, M., Lopes, V., Égüez, N., Hoffman, D.L., Benson, A., Cabanes, D., García-Targa, J., Fullola, J.M., 2021. A new chronological framework and site formation history for Cova del Gegant (Barcelona): Implications for neanderthal and anatomically modern human occupation of NE Iberian Peninsula. Quat. Sci. Rev. 270, 107141.
Demuro, M., Arnold, L.J., Parés, J.M., Pérez-González, A., Ortega, A.I., Arsuaga, J.L., Bermúdez De Castro, J.M., Carbonell, E., 2014. New luminescence ages for the Galería Complex archaeological site: Resolving chronological uncertainties on the Acheulean record of the Sierra de Atapuerca, Northern Spain. PLoS One 9 (10), e110169.
Demuro, M., Arnold, L.J., Parés, J.M., Sala, R., 2015. Extended-range luminescence chronologies suggest potentially complex bone accumulation histories at the Early-to-Middle Pleistocene palaeontological site of Huéscar-1 (Guadix-Baza basin, Spain). Quat. Int. 389, 191–212.
Demuro, M., Arnold, L.J., Aranburu, A., Gómez-Olivencia, A., Arsuaga, J.L., 2019a. Single-grain OSL dating of the Middle Palaeolithic site of Galería de las Estatuas, Atapuerca (Burgos, Spain). Quat. Geochronol. 49, 254–261.
Demuro, M., Arnold, L.J., Aranburu, A., Sala, N., Arsuaga, J.L., 2019b. New bracketing luminescence ages constrain the Sima de los Huesos hominin fossils (Atapuerca, Spain) to MIS 12. J. Hum. Evol. 131, 76–95.
Demuro, M., Arnold, L.J., Duval, M., Méndez-Quintas, E., Santonja, M., Pérez-González, A., 2020a. Refining the chronology of Acheulean deposits at Porto Maior in the river Miño basin (Galicia, Spain) using a comparative luminescence and ESR dating approach. Quat. Int. 556, 96–112.
Demuro, M., Duval, M., Arnold, L.J., Spooner, N.A., Creighton, D.F., Méndez-Quintas, E., Santonja, M., Pérez-González, A., 2020b. Insights into the relationship between luminescence and ESR dating signals from Spanish sedimentary quartz samples of different geologic origins. Quat. Int. 556, 165–179.
Demuro, M., Arnold, L.J., Parés, J.M., Aranburu, A., Huguet, R., Vallverdú, J., Arsuaga, J. L., Bermúdez de Castro, J.M., Carbonell, E., 2022. Extended-range luminescence chronologies for the Middle Pleistocene units at the Sima del Elefante archaeological site (Sierra de Atapuerca, Burgos, Spain). Quat. Geochronol. 71, 101318.
Demuro, M., Arnold, L.J., González-Urquijo, J., Lazuen, T., Frochoso, M., 2023. Chronological constraint of Neanderthal cultural and environmental changes in southwestern Europe. MIS 5–MIS 3 dating of the Axlor site (Biscay, Spain). J. Quat. Sci. 38, 890–920.
d'Errico, F., Vanhaeren, M., 2015. Upper palaeolithic mortuary practices: reflection of ethnic affiliation, social complexity, and cultural turnover. In: Renfrew, C., Boyd, M. J., Morley, I. (Eds.), Death Rituals, Social Order and the Archaeology of Immortality in the Ancient World. Cambridge University Press, pp. 45–62.
Domínguez-Villar, D., Carrasco, R.M., Pedraza, J., Cheng, H., Edwards, R.L., Willenbring, J.K., 2013. Early maximum extent of paleoglaciers from Mediterranean mountains during the last glaciation. Sci. Rep. 3, 2034.
Domínguez-Villar, D., Lojen, S., Krklec, K., Baker, A., Fairchild, I.J., 2015. Is global warming affecting cave temperature? Experimental and model data from a paradigmatic case study. Clim. Dynam. 45, 569–581.
Duarte, C., Mauricio, J., Pettitt, P.B., Souto, P., Trinkaus, E., van der Plicht, H., Zilhão, J., 1999. The early Upper Paleolithic human skeleton from the Abrigo do Lagar Velho (Portugal) and modern human emergence in Iberia. Proc. Natl. Acad. Sci. USA 96, 7604–7609.
Duval, M., Grün, R., 2016. Are published ESR dose assessments on fossil tooth enamel reliable? Quat. Geochronol. 31, 19–27.
Duval, M., Arnold, L.J., 2013. Field gamma dose-rate assessment in natural sedimentary contexts using $LaBr_3$(Ce) and NaI(Tl) probes: a comparison between the "threshold" and "windows" techniques. Appl. Radiat. Isot. 74, 36–45.
Duval, M., Arnold, L., Guilarte, V., Demuro, M., Santonja, M., Pérez-Gonzalez, A., 2017. Electron Spin Resonance dating of optically bleached quartz grains from the Middle Palaeolithic site of Cuesta de la Bajada (Spain) using the multiple centres approach. Quat. Geochronol. 37, 82–96.
Duval, M., Fang, F., Suraprasit, K., Jaeger, J.-J., Benammi, M., Chaimanee, Y., Iglesias Cibanal, J., Grün, R., 2019. Direct ESR dating of the Pleistocene vertebrate assemblage from khok sung locality, Nakhon Ratchasima Province, Northeast Thailand. Palaeontol. Electron. 22 (3.69), 1–25.
Duval, M., Arnold, L.J., Demuro, M., Parés, J.M., Campaña, I., Carbonell, E., Bermúdez de Castro, J.M., 2022. New chronological constraints for the lowermost stratigraphic unit of Atapuerca Gran Dolina (Burgos, N Spain). Quat. Geochronol. 71, 101292.
Eggins, S., Grün, R., Pike, A.W.G., Shelley, M., Taylor, L., 2003. ^{238}U, ^{232}Th profiling and U-series isotope analysis of fossil teeth by laser ablation-ICPMS. Quat. Sci. Rev. 22, 1373–1382.
Eggins, S.M., Grün, R., McCulloch, M.T., Pike, A.W.G., Chappell, J., Kinsley, L., Mortimer, G., Shelley, M., Murray-Wallace, C.V., Spötl, C., Taylor, L., 2005. In situ U-series dating by laser-ablation multi-collector ICPMS: new prospects for Quaternary geochronology. Quat. Sci. Rev. 24, 2523–2538.
Fusco, D.A., Arnold, L.J., Gully, G.A., Levchenko, V.A., Jacobsen, G.E., Prideaux, G.J., 2023. Revisiting the late quaternary fossiliferous infills of cathedral cave, wellington caves (central eastern new South Wales, Australia). J. Quat. Sci. 38, 505–525.
Galbraith, R., 2003. A simple homogeneity test for estimates of dose obtained using OSL. Ancient TL 21, 75–77.
Galbraith, R.F., Roberts, R.G., Laslett, G.M., Yoshida, H., Olley, J.M., 1999. Optical dating of single and multiple grains of quartz from Jinmium rock shelter, northern Australia: part I, experimental design and statistical models. Archaeometry 41, 339–364.
González-Sampériz, P., Gil-Romera, G., García-Prieto, E., Aranbarri, J., Moreno, A., Morellón, M., Sevilla-Callejo, M., Leunda, M., Santos, L., Franco-Múgica, F., Andrade, A., Carrión, J.S., Valero-Garcés, B.L., 2020. Strong continentality and effective moisture drove unforeseen vegetation dynamics since the last interglacial at inland Mediterranean areas: the Villarquemado sequence in NE Iberia. Quat. Sci. Rev. 242, 106425.
Grün, R., 1989. Electron spin resonance (ESR) dating. Quat. Int. 1, 65–109.
Grün, R., 2009. The DATA program for the calculation of ESR age estimates on tooth enamel. Quat. Geochronol. 4, 231–232.
Grün, R., Chadam, J., Schwarcz, H.P., 1988. ESR dating of tooth enamel: coupled correction for U-uptake and U-series disequilibrium. Nucl. Tracks 14, 237–241.
Grün, R., Eggins, S., Kinsley, L., Mosely, H., Sambridge, M., 2014. Laser ablation U-series analysis of fossil bones and teeth. Palaeogeogr. Palaeoclimatol. Palaeoecol. 416, 150–167.
Grün, R., McDermott, F., 1994. Open system modelling for U-series and ESR dating of teeth. Quat. Sci. Rev. 13, 121–125.
Guérin, G., Mercier, M., Adamiec, G., 2011. Dose-rate conversion factors: update. Ancient TL 29, 5–8.
Hocknull, S.A., Lewis, R., Arnold, L.J., Pietsch, T., Joannes-Boyau, R., Price, G.J., Moss, P., Wood, R., Dosseto, A., Louys, J., Olley, J., Lawrence, R.A., 2020. Extinction of eastern Sahul megafauna coincides with sustained environmental deterioration. Nat. Commun. 11, 2250.
Jacobs, Z., Duller, G.A.T., Wintle, A.G., Henshilwood, C.S., 2006. Extending the chronology of deposits at Blombos Cave, South Africa, back to 140 ka using optical dating of single and multiple grains of quartz. J. Hum. Evol. 51, 255–273.
Lewis, R., Tibby, J., Arnold, L.J., Barr, C., Marshall, J., McGregor, G., Gadd, P., Yokoyama, Y., 2020. Insights into subtropical Australian aridity from Welsby Lagoon, north Stradbroke Island, over the past 80,000 years. Quat. Sci. Rev. 234, 106262.
Lisiecki, L.E., Raymo, M.E., 2005. A Pliocene-Pleistocene stack of 57 globally distributed benthic $\delta^{18}O$ records. Paleoceanography 20, PA1003.
Martin, L., Mercier, N., Incerti, S., 2015. DosiVox: Implementing Geant 4-based software for dosimetry simulations relevant to luminescence and ESR dating techniques. Ancient TL 33, 1–10.
Mejdahl, V., 1979. Thermoluminescence dating: beta-dose attenuation in quartz grains. Archaeometry 21, 61–72.
Mejdahl, V., 1987. Internal radioactivity in quartz and feldspar grains. Ancient TL 5, 10–17.
Murray, A., Arnold, L.J., Buylaert, J.-P., Guérin, G., Qin, J., Singhvi, A.K., Smedley, R., Thomsen, K.J., 2021. Optically stimulated luminescence dating using quartz. Nat. Rev. Methods Primers 1, 72.
Olley, J.M., Caitcheon, G.G., Roberts, R.G., 1999. Origin of dose distributions in fluvial sediments, and the prospect of dating single grains from fluvial deposits using optically stimulated luminescence. Radiat. Meas. 30, 207–217.
Pawley, S.M., Bailey, R.M., Rose, J., Moorlock, B.S.P., Hamblin, R.J.O., Booth, S.J., Lee, J.R., 2008. Age limits on Middle Pleistocene glacial sediments from OSL dating, north Norfolk, UK. Quat. Sci. Rev. 27, 1363–1377.
Pérez-Díaz, S., López-Sáez, J.A., 2021. Late Pleistocene environmental dynamics and human occupation in Southwestern Europe. Quat. Int. 595, 39–53.
Pettitt, P.B., van der Plicht, H., Bronk Ramsey, C., Monge Soares, A.M., Zilhão, J., 2002. Chapter 7: the radiocarbon chronology. In: Zilhão, J., Trinkaus, E. (Eds.), Portrait of the Artist as a Child. The Gravettian Human Skeleton from the Abrigo Do Lagar Velho and its Archaeological Context. Instituto Português de Arqueologia 22, Lisboa, Portugal, pp. 132–138.
Pettitt, P.B., Davies, W., Gamble, C.S., Richards, M.B., 2003. Palaeolithic radiocarbon chronology: quantifying our confidence beyond two half-lives. J. Archaeol. Sci. 30, 1685–1693.
Prescott, J.R., Hutton, J.T., 1994. Cosmic ray contributions to dose rates for luminescence and ESR dating: large depths and long-term time variations. Radiat. Meas. 23, 497–500.
Rasmussen, S.O., Bigler, M., Blockley, S., Blunier, T., Buchardt, B., Clausen, H., Cvijanovic, I., Dahl-Jensen, D., Johnsen, S., Fischer, H., Gkinis, V., Guillevic, M., Hoek, W., Lowe, J., Pedro, J., Popp, T., Seierstad, I., Steffensen, J., Svensson, A., Vallelonga, P., Vinther, B., Walker, M., Wheatley, J.J., Winstrup, M., 2014. A stratigraphic framework for abrupt climatic changes during the Last Glacial period based on three synchronized Greenland ice-core records: refining and extending the INTIMATE event stratigraphy. Quat. Sci. Rev. 106, 14–28.
Rebollo, N.R., Weiner, S., Brock, F., Meignen, L., Goldberg, P., Belfer-Cohen, A., Bar-Yosef, O., Boaretto, E., 2011. New radiocarbon dating of the transition from the Middle to the upper paleolithic in Kebara cave, Israel. J. Archaeol. Sci. 38, 2424–2433.
Rees-Jones, J., 1995. Optical dating of young sediments using fine-grain quartz. Ancient TL 13, 9–14.
Rees-Jones, J., Tite, M.S., 1997. Optical dating results for British archaeological sediments. Archaeometry 39, 177–187.
Reimer, P.J., Austin, W.E.N., Bard, E., Bayliss, A., Blackwell, P.G., Ramsey, C.B., Butzin, M., Cheng, H., Edwards, R.L., Friedrich, M., Grootes, P.M., Guilderson, T.P.,

Hajdas, I., Heaton, T.J., Hogg, A.G., Hughen, K.A., Kromer, B., Manning, S.W., Muscheler, R., Palmer, J.G., Pearson, C., van der Plicht, J., Reimer, R.W., Richards, D.A., Scott, E.M., Southon, J.R., Turney, C.S.M., Wacker, L., Adolphi, F., Buntgen, U., Capano, M., Fahrni, S.M., Fogtmann-Schulz, A., Friedrich, R., Kohler, P., Kudsk, S., Miyake, F., Olsen, J., Reinig, F., Sakamoto, M., Sookdeo, A., Talamo, S., 2020. The IntCal20 Northern Hemisphere radiocarbon age calibration curve (0–55 cal kBP). Radiocarbon 62, 725–757.

Rios-Garaizar, J., Iriarte, E., Arnold, L.J., Sánchez-Romero, L., Marín-Arroyo, A.B., San Emeterio, A., Gómez-Olivencia, A., Pérez-Garrido, C., Demuro, M., Campaña, I., Bourguignon, L., Benito-Calvo, A., Iriarte, M.J., Aranburu, A., Arranz, A., Garate, D., Silva, M., Lahaye, C., Ortega, I., 2022. The intrusive nature of the châtelperronian in the Iberian Peninsula. PLoS One 17, e0265219.

Sánchez Goñi, M.F., Harrison, S.P., 2010. Millennial-scale climate variability and vegetation changes during the Last Glacial: Concepts and terminology. Quat. Sci. Rev. 29, 2823–2827.

Sanz, M., Daura, D., Costa, A.M., Araújo, A.C., 2023. The characterization of bearded vulture (*Gypaetus barbatus*) coprolites in the archaeological record. Sci. Rep. 13, 57.

Shao, Q., Bahain, J.-J., Dolo, J.-M., Falguères, C., 2014. Monte Carlo approach to calculate US-ESR age and age uncertainty for tooth enamel. Quaternary Geochronology 22, 99–106.

Shao, Q., Bahain, J.-J., Falguères, C., Dolo, J.-M., Garcia, T., 2012. A new U-uptake model for combined ESR/U-series dating of tooth enamel. Quat. Geochronol. 10, 406–411.

Straus, L.G., 2015. The human occupations of southwestern Europe during the last glacial maximum: Solutrean cultural adaptations in France and Iberia. J. Anthropol. Res. 71, 465–492.

Straus, L.G., 2018. The upper Paleolithic of Iberia. Trab. Prehist. 75, 9–51.

Talamo, S., Fewlass, H., Maria, R., Jaouen, K., 2021. "Here we go again": the inspection of collagen extraction protocols for ^{14}C dating and palaeodietary analysis. STAR: Sci. Technol. Archaeol. Res. 7 (1), 62–77.

Tattersall, I., Schwartz, J.H., 1999. Hominids and hybrids: the place of Neanderthals in human evolution. Proc. Natl. Acad. Sci. USA 96, 7117–7119.

van Klinken, G.J., 1999. Bone collagen quality indicators for palaeodietary and radiocarbon measurements. J. Archaeol. Sci. 26, 687–695.

Vegas, J., Ruiz-Zapata, B., Ortiz, J.E., Galán, L., Torres, T., García-Cortés, A., Gil-García, M.J., Pérez-González, A., Gallardo-Millán, J.L., 2010. Identification of arid phases during the last 50 kyr Cal BP from the Fuentillejo maar lacustrine record (Campo de Calatrava Volcanic Field, Spain). J. Quat. Sci. 25, 1051–1062.

Wolf, D., Kolb, T., Alcaraz-Castaño, M., Heinrich, S., Baumgart, P., Calvo, R., Sánchez, J., Ryborz, K., Schäfer, I., Bliedtner, M., Zech, R., Zöller, L., Faust, D., 2018. Climate deteriorations and Neanderthal demise in interior Iberia. Sci. Rep. 8, 7048.

Wolf, D., Kolb, T., Ryborz, K., Heinrich, S., Schäfer, I., Calvo, R., Sánchez, J., Hambach, U., Zech, R., Zöller, L., Faust, D., 2021. Evidence for strong relations between the upper Tagus loess formation (central Iberia) and the marine atmosphere off the Iberian margin during the last glacial period. Quat. Res. 101, 84–113.

Wood, R.E., Barroso-Ruíz, C., Caparrós, M., Jordá Pardo, J.F., Santos, B.G., Higham, T.F. G., 2013. Radiocarbon dating casts doubt on the late chronology of the Middle to Upper Palaeolithic transition in southern Iberia. Proc. Natl. Acad. Sci. U.S.A. 110, 2781–2786.

Zilhão, J., Trinkaus, E., 2002. Portrait of the Artist as a Child. The Gravettian Human Skeleton from the Abrigo Do Lagar Velho and its Archeological Context. Instituto Portugués de Arqueología, Trabalhos de Arqueologia 22, Lisboa, Portugal.

Zilhão, J., Angelucci, D.E., Araújo Igreja, M., Arnold, L.J., Badal, E., Callapez, P., Cardoso, J.L., d'Errico, F., Daura, J., Demuro, M., Deschamps, M., Dupont, C., Gabriel, S., Hoffmann, D.L., Legoinha, P., Matias, H., Monge Soares, A.M., Nabais, M., Portela, P., Queffelec, A., Rodrigues, F., Souto, P., 2020. Last interglacial Iberian Neandertals as Fisher-Hunter-Gatherers. Science 367, 1443.

Zilhão, J., Angelucci, D.E., Arnold, L.J., Demuro, M., Hoffmann, D.L., Pike, A.W.G., 2021a. A revised, Last Interglacial chronology for the Middle Palaeolithic sequence of Gruta da Oliveira (Almonda karst system, Torres Novas, Portugal). Quat. Sci. Rev. 258, 106885.

Zilhão, J., Angelucci, D.E., Arnold, L.J., d'Errico, F., Dayet, L., Demuro, M., Deschamps, M., Fewlass, H., Gomes, L., Linscott, B., Matias, H., Pike, A.W.G., Steier, P., Talamo, S., Wild, E.M., 2021b. Revisiting the Middle and upper Palaeolithic archaeology of Gruta do Caldeirão (Tomar, Portugal). PLoS One 16, e0259089.